RSC Advances

PAPER

View Article Online
View Journal | View Issue

Cite this: *RSC Adv.*, 2026, **16**, 30310

Facile electrochemical fabrication of GO@ZnO@MnO_2 nanocomposite for catalytic ozonation of ciprofloxacin: experimental optimization and machine learning modeling

Huu-Tap Van,[a] Le Phuong Hoang,[b] Van Hung Hoang,[a] Thi Hong Vien Nguyen,[c] Thi Dong Nguyen,[c] Thi Hong Huyen Chu,[c] Thu Huyen Nguyen,[c] Vu Thi Thuy Trang,[b] Van-Truong Nguyen[d] and Thi Minh Phuong Nguyen *[ef]

The persistence of ciprofloxacin (CIP), a widely used fluoroquinolone antibiotic, in aquatic environments poses serious risks to ecosystems and human health due to its recalcitrance and contribution to antimicrobial resistance. Herein, a novel graphene oxide-zinc oxide-manganese dioxide (GO@ZnO@MnO_2) nanocomposite was successfully synthesized *via* a facile, one-step electrochemical exfoliation method and employed as a highly efficient heterogeneous catalyst for the ozonation of CIP. The optimal nanocomposite ratio (60 : 35 : 5) achieved 90.20% total organic carbon (TOC) removal within 50 min under mild conditions (pH 9.0, catalyst dosage 1.0 g L^{-1}, initial TOC 12.21 mg L^{-1}), representing a 2.8-fold enhancement compared with ozonation alone (32.52%). The corresponding pseudo-first-order rate constant for TOC abatement during CIP degradation was 0.0532 min^{-1}, significantly higher than those of the binary and pristine systems. Scavenger experiments indicated that hydroxyl-radical-mediated oxidation contributed significantly to CIP mineralization; however, the limited suppression (~22% decrease in k) after scavenger addition strongly suggests that surface-mediated oxidation pathways and/or direct ozone reactions also played a substantial role in the overall catalytic ozonation process. Furthermore, four machine-learning models were developed to predict TOC removal efficiency. The artificial neural network (ANN) and support vector machine (SVM) models provided the strongest predictive fit within the available experimental dataset (R^2 = 0.977 and 0.976, respectively), with reaction time identified as the most influential variable. This study presents the first integration of green electrochemical synthesis, systematic parametric optimization and high-accuracy machine-learning modeling for catalytic ozonation of CIP, offering a sustainable and predictive strategy for the efficient mineralization of recalcitrant antibiotics in wastewater.

Received 22nd February 2026
Accepted 25th May 2026

DOI: 10.1039/d6ra01551d

rsc.li/rsc-advances

Introduction

The widespread occurrence of pharmaceutical residues in aquatic environments has emerged as a critical global concern due to their persistence, potential for bioaccumulation, and contribution to the development of antibiotic resistance.[1–3] Among these contaminants, ciprofloxacin (CIP), a second-generation fluoroquinolone antibiotic extensively used in human and veterinary medicine, is frequently detected in wastewater effluents, surface waters, and even drinking water sources at concentrations ranging from ng L^{-1} to mg L^{-1}.[4,5] Its complex molecular structure, containing a quinolone core, a fluorine atom, and a piperazine ring, renders CIP highly resistant to conventional biological and physicochemical treatments, leading to incomplete removal and the formation of potentially more toxic transformation products.[6,7]

Advanced oxidation processes (AOPs), particularly ozonation, have demonstrated considerable promise for the degradation of recalcitrant organic pollutants owing to the high oxidation potential of ozone (E^0 = 2.07 V) and the generation of non-selective hydroxyl radicals (˙OH, E^0 = 2.80 V).[8,9] However, standalone ozonation often suffers from low mineralization

[a]*Center for Advanced Technology Development, Thai Nguyen University, Thai Nguyen 24000, Vietnam*
[b]*Department of Environmental Technology, Faculty of Mechanical, Electrical and Electronics Technology, TNUT – Thai Nguyen University of Technology, Thai Nguyen 24000, Vietnam*
[c]*Faculty of Natural Resources and Environment, TNU – University of Sciences, Thai Nguyen 24000, Vietnam*
[d]*Faculty of Fundamental and Applied Sciences, TNUT – Thai Nguyen University of Technology, Thai Nguyen 24000, Vietnam*
[e]*Faculty of Environmental and Natural Sciences, Duy Tan University, Da Nang 550000, Vietnam. E-mail: nguyentminhphuong@dtu.edu.vn*
[f]*Institute of Research and Development, Duy Tan University, Da Nang 550000, Vietnam*

efficiency, selective reactivity toward specific functional groups, and high energy consumption for ozone generation, which limits its practical application in complex wastewater matrices.[10,11]

To overcome these limitations, heterogeneous catalytic ozonation has gained increasing attention, as solid catalysts can significantly enhance ozone decomposition into reactive oxygen species (ROS), improve mass transfer, and promote surface-mediated reactions.[12,13] Recent studies have highlighted the effectiveness of transition metal oxides such as MnO_2, ZnO, and CeO_2, as well as carbon-based supports including graphene oxide (GO) and reduced graphene oxide, in catalytic ozonation of antibiotics.[14–16] MnO_2-based catalysts excel in redox cycling (Mn^{4+}/Mn^{3+}), enabling continuous ozone activation and reactive oxygen species (ROS) generation, while ZnO provides abundant surface hydroxyl groups and oxygen vacancies that facilitate ozone adsorption and decomposition.[12] Graphene oxide (GO), with its large specific surface area, high density of oxygen-containing functional groups, and excellent electron conductivity, serves as an ideal support to prevent nanoparticle aggregation, enhance pollutant adsorption, and accelerate interfacial electron transfer processes.[17,18]

Despite notable progress, several challenges persist. Most reported catalysts are binary composites or require complex, multi-step syntheses involving toxic chemicals and high energy input, which contradict the principles of green chemistry and sustainable engineering.[19,20] Ternary GO@ZnO@MnO_2 systems remain underexplored, particularly those prepared *via* environmentally benign, one-step electrochemical methods that integrate material synthesis and functionalization in a single process. Moreover, systematic optimization of operating parameters (pH, catalyst dosage, and pollutant concentration) and data on catalyst reusability are still limited for CIP mineralization, hindering large-scale application and process design.

Furthermore, while experimental optimization is time-consuming and resource-intensive, the integration of machine learning (ML) models to predict degradation performance and identify key influencing factors has only recently begun to receive attention in catalytic ozonation studies.[21,22] High-accuracy ML frameworks capable of capturing non-linear interactions among multiple variables remain scarce for ozone-based catalytic systems, particularly for pharmaceutical degradation processes.[23]

To address these gaps, the present study introduces a novel, green and highly efficient ternary GO@ZnO@MnO_2 nanocomposite synthesized *via* a facile one-step electrochemical exfoliation approach. This method enables simultaneous exfoliation of graphite and *in situ* anchoring of ZnO and MnO_2 nanoparticles in a single, mild, reagent-efficient process, representing a significant advancement over conventional multi-step syntheses. By systematically investigating catalyst composition, operational parameters, and catalyst reusability, and by developing and validating four advanced machine-learning models (LR, ANN, RF and SVM), this work establishes the first comprehensive framework that combines sustainable catalyst design, experimental optimization and predictive artificial intelligence for the catalytic ozonation of ciprofloxacin. The integration of these elements not only overcomes the limitations of existing binary catalysts but also provides new mechanistic insights into synergistic ROS generation within the ternary heterostructure.

The primary objectives of this work were (i) to develop and characterize an efficient, reusable ternary GO@ZnO@MnO_2 catalyst *via* a facile electrochemical route, (ii) to systematically optimize key operational parameters for maximum CIP mineralization, (iii) to establish robust ML models for rapid performance prediction and (iv) to provide mechanistic insights into the synergistic ROS generation and degradation pathways. By integrating green catalyst synthesis, experimental optimization, machine-learning prediction, and detailed mechanistic understanding, this study offers a comprehensive and practical strategy for the efficient removal of fluoroquinolone antibiotics from water, advancing sustainable catalytic ozonation technologies.

It should be noted that the present study was conducted using synthetic CIP-contaminated water under controlled laboratory conditions. This approach was selected to isolate the intrinsic catalytic ozonation behavior of GO@ZnO@MnO_2 and to evaluate the effects of key operating variables without interference from complex wastewater matrices. Therefore, the ML component of this work should be considered a preliminary process-response modelling tool for controlled conditions, rather than a directly deployable predictive model for real wastewater treatment.

Materials and methods

Chemicals

All reagents were of analytical grade and used as received without further purification. High-purity graphite rods (≥99.99%, 6 mm in diameter, 100 mm in length) were purchased from a local supplier and used as electrodes for electrochemical exfoliation. Absolute ethanol (CH_3CH_2OH, 99.99%), potassium hydroxide (KOH), ammonium nitrate (NH_4NO_3), ammonium sulfate ($(NH_4)_2SO_4$), zinc nitrate hexahydrate ($Zn(NO_3)_2 \cdot 6H_2O$), manganese nitrate tetrahydrate ($Mn(NO_3)_2 \cdot 4H_2O$), hydrochloric acid (HCl), and sodium hydroxide (NaOH) were obtained from Merck (Germany). Ciprofloxacin (CIP, ≥98%) was supplied by Sigma-Aldrich and used as the target pollutant. Double-distilled water (resistivity ≥18.2 MΩ cm) was used throughout the experiments for solution preparation and washing. Pure oxygen (99.99%) from a high-pressure cylinder served as the feed gas for ozone generation. The electrolyte solutions and metal–salt precursor solutions were freshly prepared before each synthesis.

Preparation of graphene and GO@ZnO@MnO_2 nanocomposites

Graphene (GO) was synthesized *via* a two-electrode electrochemical exfoliation method. Two high-purity graphite rods (≥99.99%, diameter 6 mm, length 100 mm) served as both anode and cathode. Before use, the rods were thoroughly washed with absolute ethanol, rinsed repeatedly with double-

distilled water and dried at 60 °C for 2 h. The electrolyte solution (500 mL) was prepared by mixing 5% KOH, 7.5% NH_4NO_3 and 7.5% $(NH_4)_2SO_4$ in a 1 : 2 : 2 volume ratio. The electrodes were positioned 4.0 cm apart with an immersion depth of 2.0 ± 0.1 cm. Electrolysis was performed at room temperature (25 ± 2 °C) under a constant voltage of 10.0 ± 0.1 V, producing a stable current of 1.70–2.00 A for 60 min with continuous magnetic stirring at 300 rpm. After electrolysis, the resulting graphene suspension was collected by vacuum filtration through a 0.2 μm PVDF membrane (47 mm diameter), washed extensively with double-distilled water to remove residual electrolyte, and dried at 80 °C for 24 h. The obtained material was labeled as Gr and stored in a desiccator.

The GO@ZnO and GO@ZnO@MnO_2 nanocomposites were prepared using the same electrochemical procedure with *in situ* incorporation of metal oxides. During electrolysis, aqueous solutions of $Zn(NO_3)_2 \cdot 6H_2O$ (0.06 M) and $Mn(NO_3)_2 \cdot 4H_2O$ (0.02 M) were added dropwise from two separate burettes into the electrolyte at controlled rates corresponding to the desired nominal mass ratios. A series of nanocomposites with designed GO : ZnO : MnO_2 mass ratios of 100 : 0 : 0, 60 : 40 : 0, 60 : 35 : 5 and 60 : 30 : 10 were synthesized. These ratios refer to the mass ratios of GO, ZnO and MnO_2 used during material preparation, not to oxide phase ratios determined from EDX or XRD analysis. All other parameters (voltage, current, stirring, temperature, and reaction time) remained identical to those used for pure graphene. The final products were collected, washed, and dried following the same protocol as described above. The synthesized materials were denoted according to their nominal compositions (*e.g.*, GO@ZnO@MnO_2 60 : 35 : 5). It should be noted that the actual final composition may deviate from these designed mass ratios owing to the dynamic nature of the electrochemical process. Therefore, the ratios 60 : 35 : 5 and 60 : 30 : 10 are used throughout the study only as synthesis-based sample labels. The preparation procedure was adapted and modified from the method reported by Sun *et al.* (2022).[24]

Experimental procedure

Ciprofloxacin degradation experiments were performed in a semi-batch reactor configuration (Fig. 1). All degradation experiments were conducted using synthetic CIP-contaminated water prepared in deionized/distilled water. Ozone was continuously generated from a laboratory-scale ozone generator (Vietzone 20P, Vietzone Ozone Generator Joint Stock Company, Vietnam) using pure oxygen supplied from a high-pressure cylinder as the feed gas. Under the operating conditions used in this study, the ozone generator delivered a stable, effective ozone dosage of 1.383 g h^{-1} into the reaction system. The ozone gas stream was introduced at the bottom of a cylindrical glass reactor (height 700 mm, internal diameter 60 mm) through a fine-porosity ceramic diffuser to ensure uniform bubble distribution.

A systematic parametric study was conducted to assess the influence of key operating variables on total organic carbon (TOC) removal efficiency during catalytic ozonation of ciprofloxacin using the ternary GO@ZnO@MnO_2 nanocomposite. The

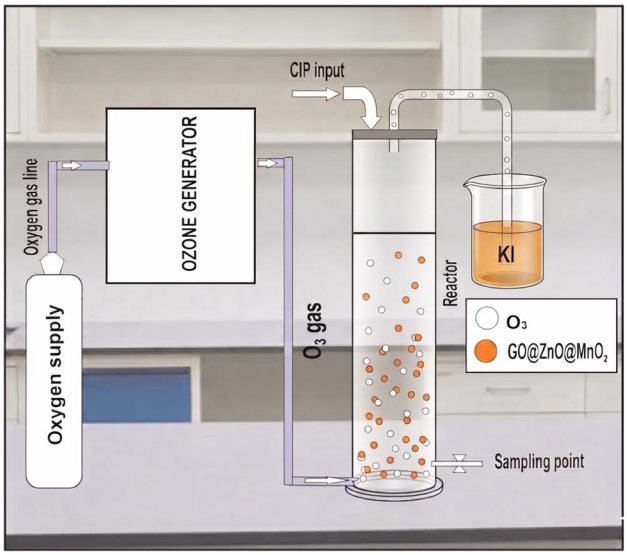

Fig. 1 Schematic diagram of the catalytic ozonation experimental setup for CIP degradation.

effect of catalyst composition was first examined by comparing pristine GO, binary GO@ZnO (60 : 40), and two ternary formulations – GO@ZnO@MnO_2 (60 : 35 : 5) and GO@ZnO@MnO_2 (60 : 30 : 10) – to identify the optimal metal-oxide ratio for TOC abatement performance. Subsequent experiments evaluated the impact of solution pH (ranging from 3.0 to 11.0) on degradation kinetics, adjusted with 0.1 M HCl or 0.1 M NaOH. Catalyst dosage was varied over the range 0.25–2.0 g L^{-1} to determine the optimal loading that provided the highest TOC abatement without inducing particle agglomeration or radical scavenging.

All runs were carried out in 500 mL of aqueous ciprofloxacin solution at ambient temperature. Ozone was continuously bubbled through the suspension, and 5 mL aliquots were withdrawn at 5-minute intervals for immediate TOC analysis. The total reaction duration for each experiment was 50 minutes. Before each run, the reactor and associated tubing were thoroughly rinsed with ultrapure water to eliminate residual contaminants.

Metal leaching analysis: to evaluate the chemical stability of the GO@ZnO@MnO_2 catalyst and the potential risk of secondary metal contamination, the treated solution was analyzed for metal leachates after catalytic ozonation. The concentrations of dissolved Zn and Mn were quantified using inductively coupled plasma optical emission spectroscopy (ICP-OES). The measured Zn and Mn concentrations were used to assess the extent of metal release from the composite catalyst after reaction.

Machine learning modeling and performance evaluation

To improve the accuracy and reliability of predictions for total organic carbon (TOC) removal during catalytic ozonation of ciprofloxacin with the GO@ZnO@MnO_2 nanocomposite, a comprehensive machine-learning workflow was developed in RStudio. Before model training, the choice of performance

metric and the selection of the most relevant input variables were carefully considered. In this study, TOC removal efficiency (%) was the primary response variable, while the four key descriptors were initial solution pH, catalyst dosage (g L^{-1}), initial TOC concentration (mg L^{-1}), and reaction time (min). Although a single evaluation metric may not capture every aspect of model quality, the combined use of R^2, RMSE and MAE provided a preliminary assessment of model fitting performance within the investigated experimental domain.

Four supervised regression algorithms – linear regression (LR), artificial neural network (ANN), random forest (RF) and support vector machine (SVM) – were constructed to forecast TOC removal efficiency in the O_3/GO@ZnO@MnO_2 system. The ANN was implemented as a relatively simple feed-forward regression model for comparative modeling rather than as a deep neural network. Given the limited dataset size, the ANN architecture was kept intentionally simple to reduce the risk of excessive parameterization and overfitting. All models were implemented in R (version 4.5.2, R Core Team, 2026). The complete dataset consisted of 160 experimental observations, each defined by the four input features and the corresponding TOC removal percentage. The ML dataset consisted of 160 time-resolved experimental observations obtained from batch catalytic ozonation experiments under different operating conditions. The input variables included pH, reaction time, initial TOC concentration, and catalyst dosage. All observations used for ML modeling were obtained from experiments performed with the optimized GO@ZnO@MnO_2 (60 : 35 : 5) catalyst. For preliminary exploratory modeling, the dataset was partitioned into a training subset (80%, 128 observations) and a testing subset (20%, 32 observations) using stratified random sampling (caret::createDataPartition, seed = 42) to preserve the distribution of the target variable. Catalyst composition was not included as an input variable in the present ML models because the composition-dependent experiments were limited to a small number of formulations and were not performed as a balanced factorial dataset across all operating conditions. Therefore, the current ML framework was designed to model the effect of operating parameters on TOC removal for the optimized catalyst, rather than to establish catalyst structure–performance relationships.

Feature scaling was performed with the caret::preProcess function. For LR, RF, and ANN, predictors were centered and scaled to a mean of 0 and a variance of 1. For SVM, min–max normalization to the [0, 1] range was applied because SVM is sensitive to the numerical scale of input variables, particularly when kernel-based distance calculations are used. This normalization ensured that variables with larger numerical ranges, such as reaction time or initial CIP/TOC concentration, did not dominate the model-fitting process solely because of their original units. The same train/test split, random seed, and evaluation metrics were retained for all models to ensure a consistent comparative modeling framework. Because the dataset was derived from time-resolved batch reaction profiles, individual observations from the same trajectory may exhibit temporal autocorrelation and therefore may not be fully independent. The random split used in this study should therefore be interpreted as a practical partitioning strategy for preliminary response-surface modeling within the investigated experimental domain, rather than as a strict trajectory-independent validation design. The relatively small dataset size also increases the risk of overfitting for flexible nonlinear models, especially ANN and SVM. Therefore, the reported model performance was interpreted as preliminary fitting performance within the available dataset, rather than definitive evidence of strong generalization to new independent experiments.

Model performance was quantitatively assessed on both training and test sets using three complementary statistical metrics: the coefficient of determination (R^2), root-mean-square error (RMSE) and mean absolute error (MAE). Reproducibility was ensured by fixing the random seed at 42 throughout all procedures. To screen for possible overfitting or underfitting, model performance on the training and testing subsets was compared using the same evaluation metrics. Large discrepancies between training and test performance were considered indicative of overfitting, whereas uniformly poor performance across both subsets was interpreted as underfitting.

The coefficient of determination (R^2) represents the proportion of variance in observed TOC removal values explained by the model; values closer to 1.0 indicate superior goodness-of-fit. The RMSE quantifies the standard deviation of the residuals (prediction errors) and is particularly sensitive to larger deviations. At the same time, the MAE provides a more interpretable linear measure of average error magnitude. The mathematical expressions for these metrics are given below:[25]

$$R^2 = 1 - \frac{\sum_{i=1}^{n}\left(y_i - \hat{y}_i\right)^2}{\sum_{i=1}^{n}\left(y_i - \bar{y}\right)^2} \quad (1)$$

$$\mathrm{RMSE} = \sqrt{\frac{1}{n}\sum_{i=1}^{n}\left(y_i - \hat{y}_i\right)^2} \quad (2)$$

$$\mathrm{MAE} = \frac{1}{n}\sum_{i=1}^{n}\left|y_i - \hat{y}_i\right| \quad (3)$$

where y_i and $\hat{y}_i$ are the observed and predicted values, $\bar{y}$ is the mean of the observed data, and n is the number of observations. Collectively, these metrics enable a balanced and thorough appraisal of the model's predictive capability, supporting reliable forecasting of ciprofloxacin degradation behavior across diverse operational scenarios.

To improve model interpretability, SHAP (Shapley Additive exPlanations) analysis was performed to quantify each input variable's contribution to model predictions. SHAP values provide a model-explanation framework based on cooperative game theory, assigning each feature a contribution value for each prediction. Positive SHAP values indicate that a given feature increases the predicted TOC removal, whereas negative SHAP values indicate that the feature decreases the predicted response. A SHAP summary plot was generated to evaluate both the global importance ranking of the input variables and the direction of their effects on the predicted removal performance.

The analysis was conducted for the best-performing ML model to provide a more robust interpretation beyond conventional feature-importance ranking.

A catalyst-composition-aware ML model would require an expanded dataset including multiple catalyst formulations and relevant physicochemical descriptors, such as GO/ZnO/MnO_2 ratio, specific surface area, pore structure, crystallinity, band gap, surface functional groups and metal composition. To assess true trajectory-level generalization more rigorously, future studies should employ grouped splitting by independent batch experiments, blocked cross-validation, or leave-one-trajectory-out validation, in which all time points from the same experimental run are assigned exclusively to either the training or testing subset.

Analytical measurements and catalyst characterization

TOC concentrations were quantified using a Multi N/C 3100 TOC/TN analyzer (Analytik Jena, Germany) equipped with catalytic high-temperature combustion. The solution pH was adjusted as required by adding 0.1 M HCl or 0.1 M NaOH, and the pH was continuously monitored with a calibrated benchtop pH meter (HANNA HI 2211-02, Romania).

The morphological features and elemental distribution of the synthesized GO@ZnO@MnO_2 nanocomposite were examined by field-emission scanning electron microscopy (SEM) coupled with energy-dispersive X-ray spectroscopy (EDX) on a JSM-IT200 instrument (JEOL, Japan) operated at an accelerating voltage of 2.0 kV under various magnifications. The crystalline structure and phase purity of the nanocomposites were determined by X-ray diffraction (XRD) using a Siemens D5005 diffractometer (Cu Kα radiation, $\lambda = 1.5417$ Å) over the 2θ range of 10–80°.

LC-MS-guided assignment of ciprofloxacin transformation intermediates: to support the mechanistic interpretation of ciprofloxacin transformation during catalytic ozonation, possible degradation intermediates were assigned based on LC-MS-guided molecular ion information and structural consistency with known fluoroquinolone oxidation chemistry. Samples were collected from the O_3/GO@ZnO@MnO_2 catalytic ozonation system operated under the optimized conditions: pH 9.0, catalyst dosage of 1.0 g L^{-1}, initial TOC concentration of 12.21 mg L^{-1}, and reaction time up to 50 min. Before analysis, aliquots were withdrawn at selected time intervals, filtered through a 0.22 μm membrane to remove suspended catalyst particles, and immediately quenched to minimize further oxidation.

The apparent degradation kinetics were evaluated based on TOC abatement rather than direct CIP concentration. The TOC data were fitted using an apparent pseudo-first-order model:

$$\ln(C_t/C_0) = -k_d \times t,$$

where C_0 and C_t represent the TOC concentration at the initial time and at reaction time t, respectively, and k is the apparent pseudo-first-order rate constant for TOC abatement during CIP degradation. The k_d value was obtained from the negative slope of the linear regression plot of $\ln(C_t/C_0)$ *versus* reaction time. Because this model was derived from TOC removal, k_d should be interpreted as an apparent overall rate constant for TOC abatement/mineralization under the specified operating conditions, rather than an intrinsic rate constant for elementary CIP degradation reactions. This model was applied because the catalyst dosage was fixed during each run and ozone was continuously supplied at a stable rate, allowing ozone availability and the concentration of catalytically active sites to be treated as approximately constant over the reaction period. Therefore, k_d should be interpreted as an apparent kinetic parameter reflecting the overall catalytic ozonation rate under the specified operating conditions, rather than as an elementary reaction-rate constant.

Results and discussion

Effect of nanocomposite ratio for GO@ZnO@MnO_2 synthesis on ciprofloxacin removal by catalytic ozonation

Fig. 2 illustrates the influence of different nanocomposite ratios of GO, ZnO and MnO_2 on the catalytic ozonation efficiency for ciprofloxacin (CIP) degradation, evaluated *via* TOC removal and pseudo-first-order kinetic analysis. A clear enhancement in mineralization efficiency is observed upon incorporation of catalytic materials compared to single ozonation (O_3 alone), demonstrating the crucial role of heterogeneous catalysis in promoting ozone activation and reactive oxygen species (ROS) generation. It should be noted, however, that because the GO-containing nanocomposite may also adsorb ciprofloxacin and dissolved organic species, part of the observed TOC decrease may reflect surface uptake in addition to catalytic oxidation. Since no catalyst-only adsorption control experiment was performed under ozone-free conditions, the baseline contribution of adsorption could not be quantified directly in the present study.

Among all tested systems (Fig. 2a), the O_3/GO@ZnO@MnO_2 (60 : 35 : 5) composite exhibits the highest catalytic performance, achieving a TOC removal of 64.95% within 50 min, which is approximately 2.0-fold higher than that obtained with O_3 alone (32.52%) and significantly superior to O_3/GO@ZnO (50.13%). Although adsorption on the GO-containing surface may contribute to part of this TOC decrease, the substantial enhancement relative to ozonation alone and the higher pseudo-first-order rate constant strongly support an important role of catalytic ozone activation in the overall process. The corresponding pseudo-first-order rate constant ($k_d = 0.029$ min^{-1}, $R^2 = 0.9637$) further confirms the kinetic superiority of this composite, exceeding those of O_3 alone ($k_d = 0.010$ min^{-1}), O_3/GO@ZnO ($k_d = 0.019$ min^{-1}) and other MnO_2-containing composites (60 : 30 : 10 and 60 : 35 : 5). This performance enhancement may be associated with the combined contribution of GO, ZnO and MnO_2 in the ternary composite, including improved dispersion of metal oxide phases on GO, increased availability of catalytic surface sites and possible interfacial interactions that facilitate ozone activation. However, because individual ZnO, MnO_2 and GO@MnO_2 control catalysts were not evaluated in the present study, the specific contribution of each component and the extent of true

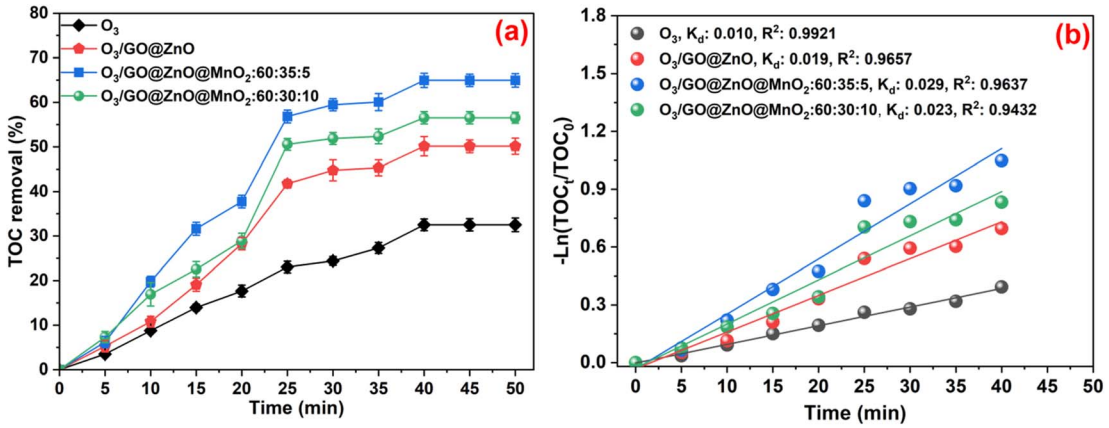

Fig. 2 Effect of various composite ratios between GO, ZnO and MnO_2 as a catalyst for ozonation processes of CIP removal (a) TOC and (b) pseudo-first-order rate constants for TOC abatement during CIP degradation at an initial TOC concentration of 12.1 mg L^{-1}; pH of 6.8; catalyst dosage of 0.5 g L^{-1} and contact time of 0–50 min.

interfacial synergy cannot be quantified definitively from the current dataset. Graphene oxide (GO) provides a high-surface-area, conductive platform that facilitates efficient electron transfer and the adsorption of CIP molecules, thereby increasing local reactant concentration at catalytically active sites.[26] ZnO provides a plethora of surface hydroxyl groups and oxygen vacancies, thereby facilitating the adsorption and decomposition of ozone into hydroxyl radicals ($^{\bullet}OH$).[27] The introduction of MnO_2, recognized for its redox-active properties, further accelerates the decomposition of ozone through Mn(IV)/Mn(III) cycling, resulting in an elevated generation of highly oxidative ROS, including $^{\bullet}OH$ and superoxide anions ($O_2^{\bullet-}$).[28] However, it is noteworthy that the catalytic performance does not increase monotonically with increasing MnO_2 content. While a moderate MnO_2 loading of 5 wt% (in the 60 : 35 : 5 ratio) markedly enhances activity, higher loadings (10 wt%) show a decline in efficiency. This trend can be attributed to phenomena such as active-site shielding, agglomeration effects, and diminished interfacial contact between GO and ZnO phases; all of which impede the efficiency of electron transfer and reduce the availability of catalytic sites.[29] Excessive MnO_2 may also obstruct ozone diffusion pathways and curtail effective surface exposure, thereby hindering radical generation efficiency.[26]

The kinetic linearity observed in Fig. 2b (R^2 > 0.94 for all systems) indicates that TOC abatement can be adequately described by an apparent pseudo-first-order model under the applied semi-batch conditions. Since the kinetic fitting was based on TOC rather than direct CIP concentration or intermediate profiles, the calculated k_{app} values should be interpreted as apparent overall mineralization constants. Therefore, no definitive rate-determining step can be assigned from these data alone. The substantially higher k_d value for the 60 : 35 : 5 composite reflects its superior ability to catalytically decompose ozone into reactive species rather than relying on direct molecular ozone oxidation, which is known to be less effective for complex fluoroquinolone structures such as CIP.[30]

Collectively, these findings indicate that the ternary GO–ZnO–MnO_2 formulation, particularly at the 60 : 35 : 5 ratio, provided the best catalytic ozonation performance among the materials tested in this study. The observed enhancement is consistent with a cooperative effect among GO, ZnO and MnO_2; however, further control experiments with individual and binary component catalysts would be required to confirm and quantify the interfacial synergy more rigorously. The ideal composite ratio of 60 : 35 : 5 achieves a favorable balance among surface area, redox activity, electron transfer competence, and interfacial synergy, culminating in enhanced ROS generation, expedited mineralization kinetics, and improved TOC removal. Hence, this specific composite ratio is the optimal formulation for synthesizing GO@ZnO@MnO_2 and is used as the catalytic agent in all subsequent experiments in this study.

Characteristics of the GO@ZnO@MnO_2 catalyst

Fig. 3 presents the SEM micrographs of GO, GO@ZnO (60 : 40), GO@ZnO@MnO_2 (60 : 35 : 5), and GO@ZnO@MnO_2 (60 : 30 : 10), revealing distinct morphological evolutions induced by sequential composite formation. The pristine GO (Fig. 3a) displays a characteristic lamellar, sheet-like structure composed of thin, stacked nanosheets, typical of exfoliated graphene oxide. This structure provides a high specific surface area and a rich array of functional groups that are conducive to the subsequent anchoring of materials.[31] Following the incorporation of ZnO (Fig. 3b), the GO sheets become partially covered by densely distributed granular and aggregated nanostructures, indicating successful nucleation and growth of ZnO particles on the GO surface. This morphology suggests strong interfacial interactions between ZnO and oxygen-containing functional groups of GO, which favor uniform dispersion and intimate contact, essential for efficient charge transfer and catalytic activity.[32]

With the introduction of MnO_2 (Fig. 3c), the GO@ZnO@MnO_2 (60 : 35 : 5) composite showcases a highly heterogeneous, hierarchical morphology characterized by well-

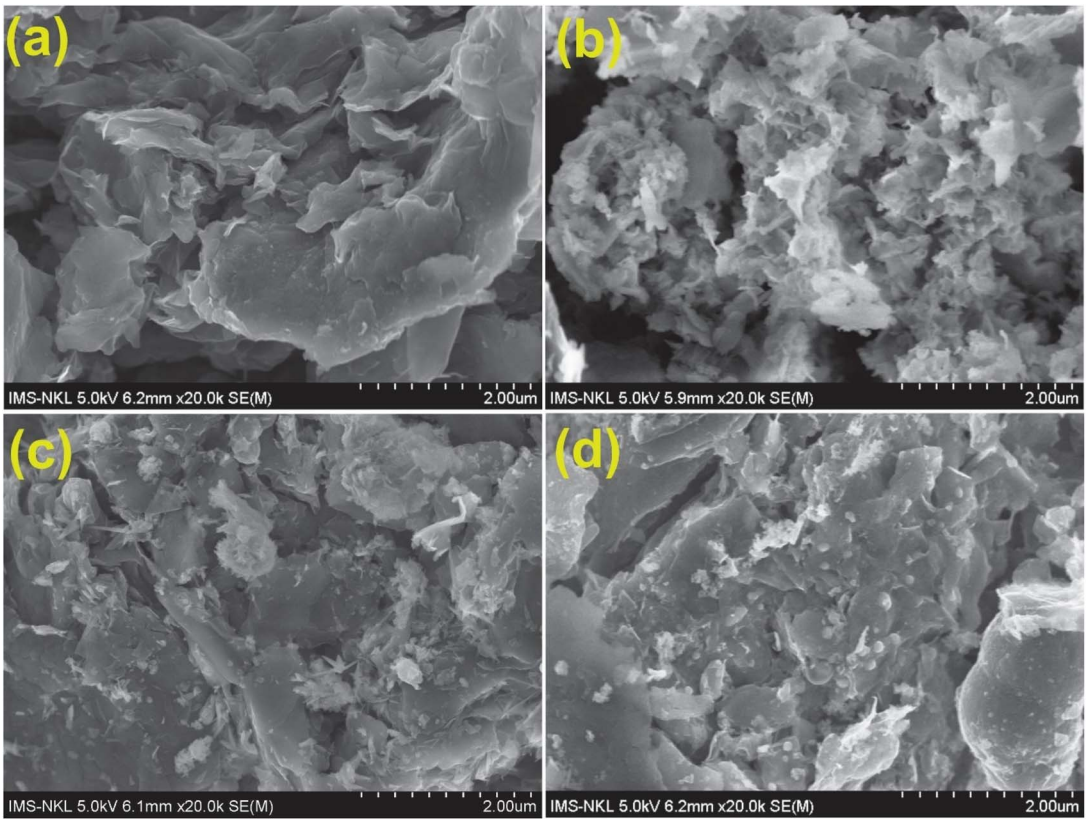

Fig. 3 SEM images of GO (a), GO@ZnO 60 : 40 (b), GO@ZnO@MnO_2 60 : 35 : 5 (c) and GO@ZnO@MnO_2 60 : 30 : 10 (d).

dispersed nanoscale clusters anchored onto the GO sheets. This multiphase heterostructured architecture enhances surface roughness, interfacial area, and defect density, producing abundant exposed active sites for ozone adsorption and activation. The intimate interfacial coupling among GO, ZnO and MnO_2 promotes efficient electron transport pathways while facilitating redox cycling processes that are vital for catalytic ozone decomposition and ROS generation.[33] In contrast, the GO@ZnO@MnO_2 (60 : 30 : 10) composite (Fig. 3d) shows a more compact, partially agglomerated morphology, where excessive MnO_2 loading leads to particle clustering and surface coverage, reducing the accessibility of active sites and weakening interfacial synergy.[34]

These morphological differences provide a clear structural explanation for the catalytic performance trends observed in Fig. 2. The optimized GO@ZnO@MnO_2 (60 : 35 : 5) composite exhibits a well-balanced hierarchical microstructure, combining high surface area, homogeneous dispersion, strong interfacial contact and efficient electron-transfer channels, which collectively facilitate ozone activation. Conversely, excessive MnO_2 incorporation disrupts this structural balance, leading to agglomeration and partial blockage of active interfaces, thereby diminishing catalytic efficiency. Therefore, the SEM analysis supports the formation of an optimized heterostructured architecture in the 60 : 35 : 5 composite, which may contribute to the superior catalytic performance observed among the tested materials. However, SEM evidence alone cannot prove interfacial synergy; additional control catalysts and surface- and interface-sensitive characterization would be needed to establish the exact origin of the catalytic enhancement.

The crystalline structures of GO, GO@ZnO with designed mass ratio (60 : 40), GO@ZnO@MnO_2 with designed mass ratio (60 : 35 : 5) and GO@ZnO@MnO_2 with designed mass ratio (60 : 30 : 10) were further investigated by X-ray diffraction (XRD), as shown in Fig. 4. Pristine GO (Fig. 4a) exhibits a broad diffraction peak centered at around $2\theta \approx 10$–$11°$, corresponding to the (001) plane of graphene oxide. This peak is indicative of the enlarged interlayer spacing caused by oxygen-containing functional groups and intercalated water molecules, thereby confirming the successful oxidation and exfoliation of graphite into GO sheets.[35] Upon the incorporation of ZnO (GO@ZnO: 60 : 40), as shown in Fig. 4b, distinct diffraction peaks appear at $2\theta \approx$ 31.7°, 34.4°, 36.2°, 47.5°, 56.6°, and 62.8°. These peaks are well-indexed to the (100), (002), (101), (102), (110), and (103) planes of the hexagonal wurtzite ZnO phase (JCPDS No. 36-1451),[36] confirming the effective formation and crystallization of ZnO on the GO matrix. The significant weakening or broadening of the characteristic GO peak suggests strong interfacial interactions and effective prevention of restacking, driven by the anchoring of ZnO nanoparticles.

With the introduction of MnO_2 in the nanocomposites (Fig. 4c and d), additional diffraction features corresponding to MnO_2 phases emerge, while the ZnO peaks retain good

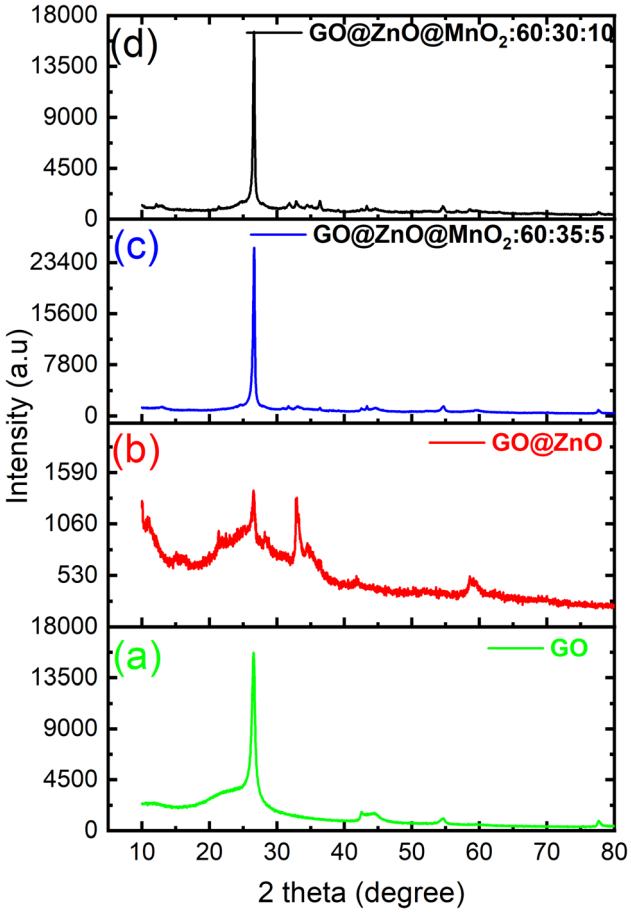

Fig. 4 XRD patterns of GO (a), GO@ZnO: 60 : 40 (b), GO@ZnO@MnO_2: 60 : 35 : 5 (c) and GO@ZnO@MnO_2: 60 : 30 : 10 (d).

visibility. This observation indicates the coexistence of multiple crystalline phases within the nanocomposite. The GO@ZnO@MnO_2 (60 : 35 : 5) sample showcases well-defined reflections of ZnO alongside weak but identifiable peaks relating to the MnO_2 phase, signifying a high dispersion and nanoscale distribution of MnO_2 across the nanocomposite surface. This finding indicates the formation of a hetero-structured multiphase nanocomposite rather than a mere physical mixture, thereby enhancing electron transfer and catalytic performance.[37] In contrast, the GO@ZnO@MnO_2 (60 : 30 : 10) sample (Fig. 4d) shows relatively enhanced intensity of the MnO_2 peaks, suggesting increased crystallite density and instances of partial aggregation, which aligns with the observations made through scanning electron microscopy (SEM). The absence of any impurity phases confirms both the high purity and successful synthesis of the engineered ternary nanocomposite system. Thus, the XRD results confirm the successful assembly of the GO@ZnO@MnO_2 heterostructure, in which crystalline ZnO and MnO_2 nanoparticles are effectively integrated onto the GO framework. This structure is expected to favor interfacial contact, redox activity, and catalytic activation of ozone; however, the exact contribution of each component to the observed performance requires further validation using additional control catalysts.

The elemental composition and spatial distribution of the synthesized nanocomposites were confirmed through energy-dispersive X-ray spectroscopy (EDX), as illustrated in Fig. 4. The EDX spectrum of pristine graphene oxide (GO) (Fig. 5a) reveals dominant peaks for C and O, consistent with the expected oxygen-rich functionalized structure of GO. This confirms the successful functionalization and oxidation of graphite into GO sheets, which is essential for further nanocomposite synthesis.[38] Subsequently, the EDX analysis of the GO@ZnO nanocomposite (Fig. 5b) shows distinct signals for Zn alongside C and O, demonstrating the successful immobilization of ZnO on the GO surface. The presence of Zn signals confirms that the synthesis process effectively incorporates ZnO into the nanocomposite matrix, thereby enhancing catalytic properties. In the nanocomposites (Fig. 5c and d), characteristic peaks corresponding to Mn are detected, in addition to the prevalent signals for C, O, and Zn. This observation confirms the successful incorporation of MnO_2 into the nanocomposite framework. The EDX spectra confirm the presence of C, O, Zn and Mn in the synthesized composites, supporting the successful incorporation of Zn- and Mn-containing phases into the GO-based matrix.[39] Moreover, the consistent detection of Zn and Mn signals across the scanned areas suggests that Zn- and Mn-containing species were distributed within the GO-supported composite, although quantitative determination of the bulk component ratio would require complementary bulk compositional analysis. This homogenous elemental integration is critical for establishing efficient interfacial charge-transfer pathways and redox-active junctions among the GO, ZnO and MnO_2 phases. Such a structural arrangement may facilitate cooperative catalytic behavior by improving contact among GO, ZnO, MnO_2 and ozone-derived reactive species.[40]

In conclusion, the results from SEM, XRD and EDX analyses robustly confirm the successful synthesis of the structurally integrated GO@ZnO@MnO_2 nanocomposite. This nanocomposite exhibits well-defined morphology, crystalline phases, and homogeneous elemental distribution. Notably, the nanocomposite prepared with the designed GO : ZnO : MnO_2 mass ratio of 60 : 35 : 5 demonstrated improved catalytic performance among the tested materials. SEM, XRD, and EDX analyses confirmed the successful formation of this ternary composition, showing well-dispersed ZnO and MnO_2 nanoparticles on the GO sheets and multiphase coexistence. These results are consistent with the superior TOC removal efficiency observed for this particular formulation.

These characteristics elucidate a direct structure–composition–function relationship, effectively linking material architecture to enhanced ozone activation, ROS generation, and improved CIP mineralization efficiency.

Effect of pH on the O_3/GO@ZnO@MnO_2 catalytic system for CIP degradation

Based on prior results, the GO@ZnO@MnO_2 nanocomposite with a designed mass ratio 60 : 35 : 5 has been identified as the

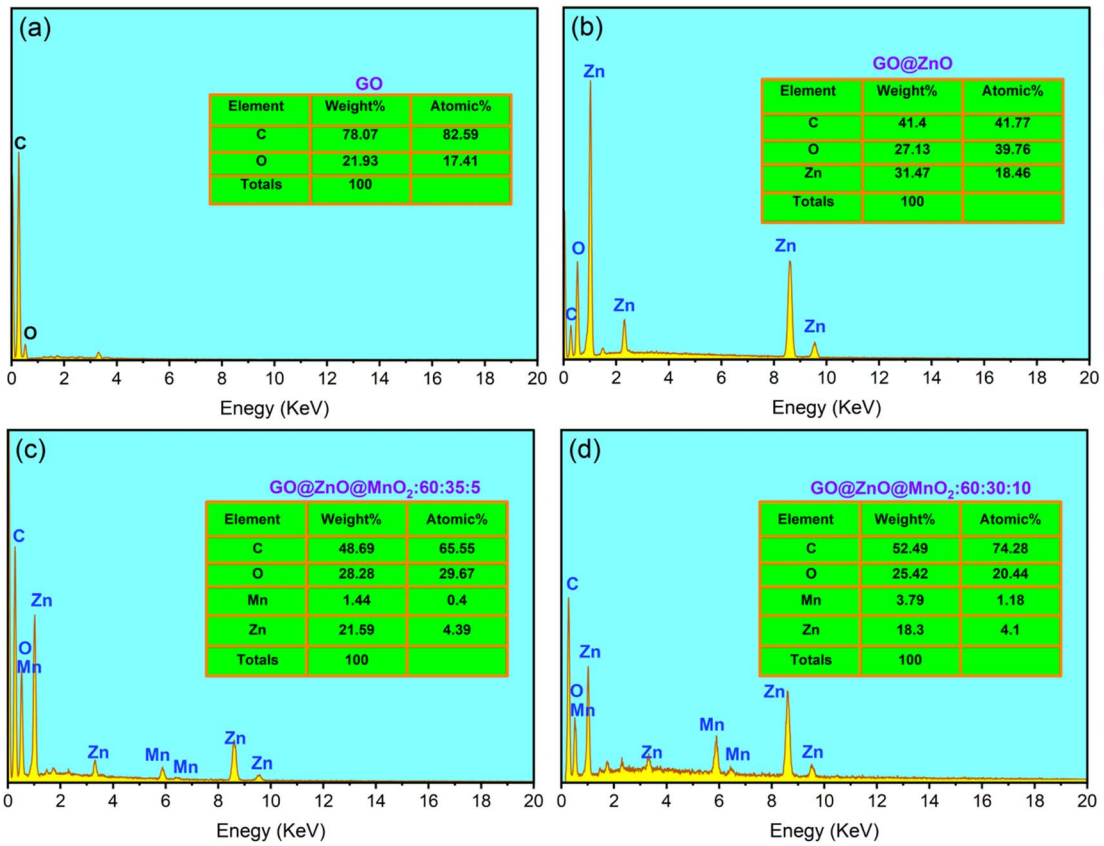

Fig. 5 EDX spectrum of GO (a), GO@ZnO: 60 : 40 (b), GO@ZnO@MnO_2: 60 : 35 : 5 (c) and GO@ZnO@MnO_2: 60 : 30 : 10 (d).

optimal catalytic material, demonstrating exceptional catalytic ozonation efficiency for CIP degradation. This optimized nanocomposite was thus selected for subsequent experiments to assess the effects of key operational parameters on catalytic performance. In particular, the influence of solution pH on CIP mineralization was systematically investigated using the O_3/GO@ZnO@MnO_2 (60 : 35 : 5) system, as depicted in Fig. 6. The pH of the solution is a crucial factor affecting ozone stability, the surface chemistry of catalysts, the speciation of pollutants, and the pathways by which reactive oxygen species (ROS) are generated in catalytic ozonation systems. Fig. 6 illustrates the impact of varying pH levels (3–11) on the mineralization performance of CIP, as evaluated by total organic carbon (TOC) removal and pseudo-first-order kinetic analysis.

A notable pH-dependent behavior emerged concerning TOC removal efficiency. The efficiency demonstrated a progressive increase from acidic to alkaline conditions, peaking at pH 9, where a TOC removal of 78.41% was achieved within 50 min (Fig. 6a). In contrast, lower efficiencies of 33.88% at pH 3, 43.99% at pH 5 and 64.05% at pH 7 were recorded. Although a comparable removal efficiency of 64.90% was achieved at pH 11, it was still substantially lower than that at pH 9, highlighting an optimal alkaline range rather than a straightforward enhancement with rising pH. The accompanying kinetic analysis (Fig. 6b) further validates this trend, revealing the highest pseudo-first-order rate constant (k_d) at pH 9 ($k_d = 0.0356\ min^{-1}$, $R^2 = 0.9638$), indicative of accelerated mineralization dynamics in moderately alkaline conditions.[41]

When examining the effects of pH alongside reaction time, distinct kinetic behaviors are observable. Under acidic conditions (pH 3 and 5), TOC removal proceeds sluggishly, registering increases of merely 4.31% and 5.79% at the 5-min mark, respectively. After 20 min, these values increased to 24.36% and 28.48%, ultimately stabilizing at low overall efficiencies of 33.88% and 43.99% after 50 min. These performances are reflected in lower k_d values of 0.0090 min^{-1} ($R^2 = 0.9292$) at pH 3 and 0.0127 min^{-1} ($R^2 = 0.9560$) at pH 5. In contrast, TOC removal accelerated moderately at neutral pH 7, achieving 37.49% by 20 min and 64.05% by 50 minutes, with a k_d of 0.0234 min^{-1} ($R^2 = 0.9764$). The most significant synergy between pH and time occurred at pH 9, where TOC removal surged to 47.21% within 20 min and approached near-saturation at 78.41% by 50 min, supported by the elevated k_d of 0.0356 min^{-1} ($R^2 = 0.9638$). Although pH 11 showed competitive initial rates (*e.g.*, 38.73% at 20 min), efficiency tapered to 64.90% at 50 min, with a k_d of 0.0232 min^{-1} ($R^2 = 0.9703$), indicating that inhibitory effects became more pronounced with extended exposure.

The mechanistic basis for this behavior can be elucidated by examining the pH-dependent pathways for ozone decomposition and catalytic reactions. In acidic conditions (pH 3–5), ozone remains relatively stable, primarily engaging in direct

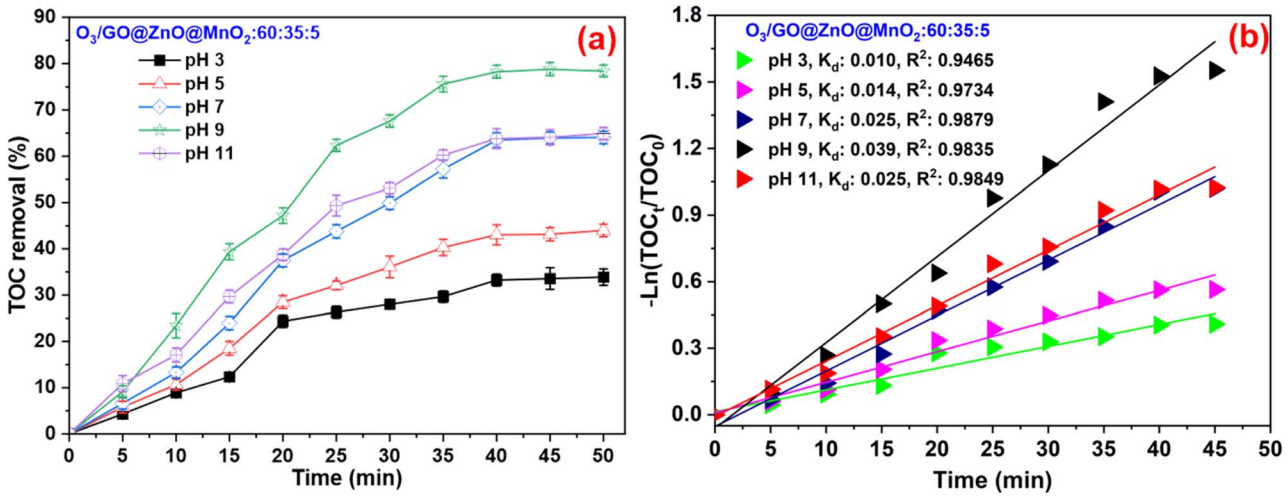

Fig. 6 Influence of pH on removal of CIP (a) TOC and (b) pseudo-first-order rate constants for TOC abatement during CIP degradation by O_3/GO@ZnO@MnO_2: 60 : 35 : 5 system at initial TOC concentration of 12.21 mg L^{-1}; pH from 3 to 11; catalyst dosage of 0.5 g L^{-1} and contact time of 0–50 min.

molecular oxidation, and exhibits limited reactivity toward complex aromatic and heterocyclic compounds such as ciprofloxacin. This scenario culminates in suboptimal mineralization efficiency, as manifested by the lower k_d and time-integrated removal rates.[42] As pH increases, base-catalyzed ozone decomposition is markedly enhanced, thereby fostering the generation of highly oxidative species, chiefly hydroxyl radicals (OH), *via* hydroxide-ion-initiated reactions. These radicals possess high non-selective reactivity and redox potentials, enabling them to efficiently cleave the CIP molecular structure, thereby promoting deep mineralization throughout the reaction timeline.[43]

At an optimal pH of 9, an advantageous equilibrium is attained between ozone stability and radical generation, maximizing ROS production and catalytic activity, aligning with the peak k_d value and strong fit to pseudo-first-order kinetics. The enhanced surface hydroxylation of the GO@ZnO@MnO_2 catalyst under alkaline conditions further amplifies the density of reactive –OH groups, which are vital to promoting ozone adsorption and activation. Synergistic interactions between ozone decomposition, augmented by the alkaline setting, and the redox-active MnO_2/ZnO heterostructure further accelerate ROS generation *via* interfacial electron transfer and Mn(IV)/Mn(III) redox cycling, contributing to the superior catalytic performance observed over the 50-minute evaluation.[44]

However, at excessively high pH (pH 11), mineralization efficiency declines even within the alkaline range. Several factors contribute to this downturn, including radical scavenging by excess hydroxide and carbonate species, which can compete for $^{\bullet}OH$ radicals and yield less reactive carbonate radicals. Furthermore, excessive alkalinity may disrupt the catalyst's surface charge, hindering CIP adsorption and interfacial kinetics. Collectively, these aspects reduce the effective availability of ROS for CIP oxidation, leading to diminished mineralization efficiency and the k_d value comparable to that at pH 7, despite the high R^2 (0.9703), reaffirming kinetic adherence.[45]

In summary, the results reaffirm that the catalytic ozonation performance of the O_3/GO@ZnO@MnO_2 system is significantly influenced by pH. Moderately alkaline conditions (approximately pH 9) provide the most favorable environment for optimal ozone activation, ROS generation, and CIP degradation, as evidenced by a k_d of 0.0356 min^{-1} (R^2 = 0.9638) and TOC removal of 78.41% after 50 min. Consequently, pH 9 was established as the ideal operational condition for all subsequent experiments in this research, ensuring maximum catalytic efficiency and consistency across evaluations.

Influence of catalyst dosage on the O_3/GO@ZnO@MnO_2 system for CIP degradation

Following the identification of pH 9 as the optimal condition for maximizing the CIP mineralization, the influence of catalyst dosage on the performance of the O_3/GO@ZnO@MnO_2 (60 : 35 : 5) system was subsequently evaluated, as illustrated in Fig. 7. Catalyst dosage represents a critical operational parameter in heterogeneous catalytic ozonation processes, as it directly impacts the availability of active surface sites for ozone adsorption and decomposition, the generation of ROS, mass transfer dynamics, and potential catalyst aggregation or self-quenching effects at elevated concentrations.

Fig. 7a shows a clear trend in TOC removal efficiency with catalyst dosage, with performance improving from 0.25 g L^{-1} to 1.0 g L^{-1}, after which a marginal decline is observed at higher dosages. At the lowest dosage of 0.25 g L^{-1}, TOC removal reached only 43.52% after 50 minutes, whereas it increased to 78.41% at 0.5 g L^{-1} and peaked at 90.20% at 1.0 g L^{-1}. Further increases to 1.5 g L^{-1} and 2.0 g L^{-1} resulted in slightly lower efficiencies of 86.77% and 86.22%, respectively. This finding indicates an optimal dosage threshold at 1.0 g L^{-1}, beyond which additional catalyst does not proportionally enhance

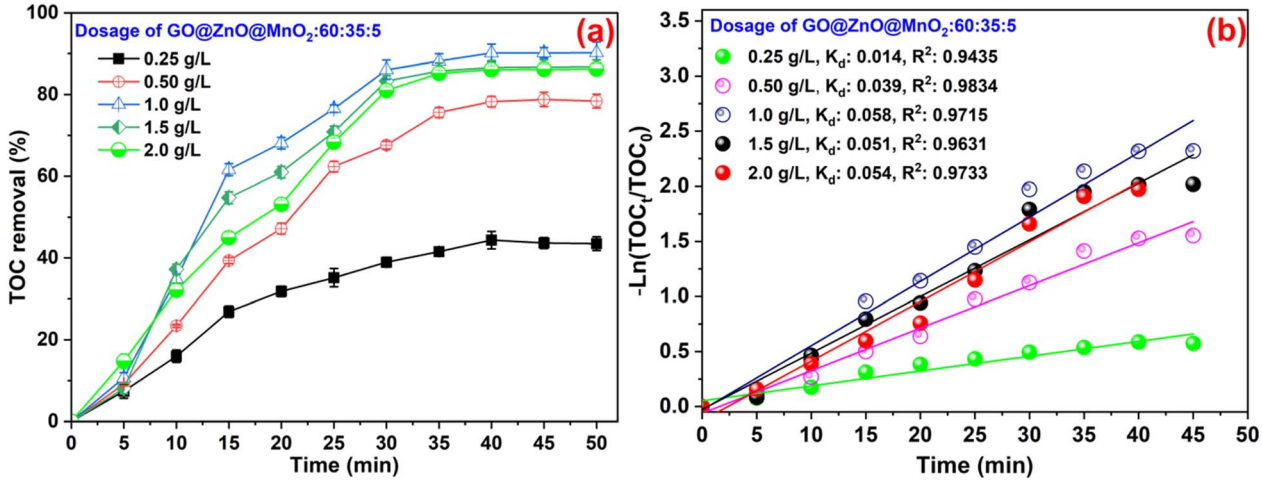

Fig. 7 Influence of GO@ZnO@MnO_2 dosage on removal of CIP (a) TOC and (b) pseudo-first-order rate constants for TOC abatement during CIP degradation by O_3/GO@ZnO@MnO_2 system at initial TOC concentration of 12.21 mg L^{-1}; pH of 9.0; catalyst dosage of 0.25–2.0 g L^{-1} and contact time of 0–50 min.

mineralization. Temporal profiles show that higher catalyst dosages accelerate initial removal rates, with substantial gains observed within 15–20 min. For instance, at 1.0 g L^{-1}, TOC removal reached 61.60% by 15 min and 68.09% by 20 min, whereas at 0.25 g L^{-1} it reached only 26.88% at 15 min and 31.82% at 20 min. This highlights the enhancement provided by an increased number of active sites in expediting early-stage ROS-mediated oxidation.[46] At the same time, the higher catalyst loading may also increase the available surface area for the adsorption of ciprofloxacin and intermediate organic species. Therefore, the observed TOC reduction should be interpreted as resulting from combined interfacial adsorption and catalytic oxidation, rather than catalytic mineralization alone, in the absence of an adsorption-only control.

The pseudo-first-order kinetic analysis in Fig. 7b reinforces the interplay between dosage and time, as the mineralization process fits well to pseudo-first-order kinetics across all tested dosages, with R^2 values ranging from 0.9104 to 0.9638. The k increased from 0.0121 min^{-1} (R^2 = 0.9104) at 0.25 g L^{-1} to a maximum of 0.0532 min^{-1} (R^2 = 0.9484) at 1.0 g L^{-1} before decreasing slightly to 0.0466 min^{-1} (R^2 = 0.9386) at 1.5 g L^{-1} and 0.0463 min^{-1} (R^2 = 0.9456) at 2.0 g L^{-1}. These observations indicate that the steepest slopes in the semi-logarithmic plots occur at 1.0 g L^{-1} during the initial 20–30 min, reflecting enhanced kinetic rates driven by abundant catalytic sites. However, at higher dosages, the plateauing after 30 minutes suggests diminishing returns, where extended reaction times do not compensate for potential inhibitory factors.[47]

Mechanistically, the observed trends can be attributed to the balance between active site availability and system limitations. At low dosages (0.25–0.5 g L^{-1}), the limited abundance of surface hydroxyl groups, oxygen vacancies in ZnO, and active redox pairs (Mn(IV)/Mn(III)) restrict ozone activation and ROS production, as evidenced by lower k values and time-integrated efficiencies, primarily driven by slower direct ozonation. As the dosage elevates to 1.0 g L^{-1}, the expanded interfacial area accommodates greater ozone decomposition, augmented electron transfer across the GO@ZnO@MnO_2 heterostructure and improved pollutant adsorption, leading to maximized ROS generation and rapid CIP breakdown over the reaction duration.[48]

This optimal dosage corresponds to a favorable catalyst-to-pollutant ratio, mitigating mass-transfer resistances and maximizing synergistic catalysis. Beyond 1.0 g L^{-1}, however, catalyst aggregation may occur, reducing effective surface area and promoting ROS self-quenching or recombination. Excess particles can inhibit dispersion, limiting the penetration of light and ozone into the suspension. Moreover, increased catalyst loading might intensify competition for ozone molecules among active sites, thereby diluting per-site efficiency and yielding comparable or lower k values despite prolonged exposure.[49]

In summary, the catalytic ozonation efficiency in the O_3/GO@ZnO@MnO_2 system shows a strong dependence on catalyst dosage, with an optimum at 1.0 g L^{-1}. This dosage achieves the highest TOC removal of 90.20% after 50 min and a corresponding pseudo-first-order rate constant of 0.0532 min^{-1} (R^2 = 0.9484). Thus, this optimized dosage was selected for subsequent evaluations, balancing performance enhancements with practical considerations, including material consumption and process economics in the treatment of antibiotic-laden wastewater.

Effect of CIP concentration

Following the establishment of pH 9 and a catalyst dosage of 1.0 g L^{-1} as the optimal conditions for maximizing the CIP mineralization, the impact of initial CIP concentration on the performance of the O_3/GO@ZnO@MnO_2 (60 : 35 : 5) system was evaluated, as illustrated in Fig. 8. The initial concentration of the pollutant is a critical factor in advanced oxidation processes, influencing the ratio of ROS to substrate molecules, the

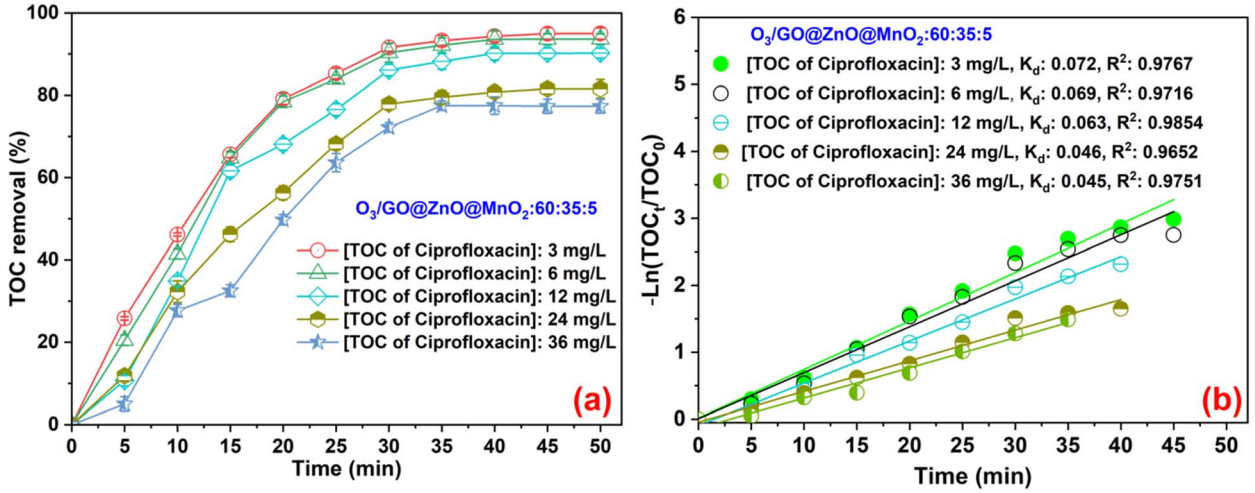

Fig. 8 Influence of CIP concentration on removal by O_3/GO@ZnO@MnO_2 system (a) TOC and (b) pseudo-first-order rate constants for TOC abatement during CIP degradation at initial TOC concentration of 3–36 mg L^{-1}; pH of 9.0, catalyst dosage of 1.0 g L^{-1} and contact time of 0–50 min.

adsorption equilibria on the catalyst surface, and the potential accumulation of intermediate or competitive inhibition effects.

Fig. 8a shows a clear inverse relationship between initial CIP concentration (ranging from 3 to 36 mg L^{-1}) and TOC removal efficiency, with higher concentrations correlating with lower TOC removal percentages over the 50-min reaction period. At the lowest concentration of 3 mg L^{-1}, an impressive 94.97% TOC removal was achieved within 50 min, compared to 93.63% at 6 mg L^{-1} (TOC), 90.20% at 12 mg L^{-1}, 81.57% at 24 mg L^{-1}, and 77.33% at 36 mg L^{-1}. These results illustrate that lower pollutant concentrations allow for faster and more complete degradation due to greater ROS availability relative to the pollutant load.[50] The temporal profiles show rapid initial mineralization across all concentrations, with the majority of TOC removal occurring within 20–30 min. At 3 mg L^{-1}, TOC removal reached 79.14% after 20 min and 91.59% after 30 min. In contrast, at the highest concentration of 36 mg L^{-1}, the removal was more gradual, progressing to only 49.73% by 20 min and 72.19% by 30 min. This discrepancy emphasizes that lower concentrations facilitate more efficient degradation due to the ample availability of ROS relative to the amount of pollutant present.[51]

The pseudo-first-order kinetic analysis presented in Fig. 8b further corroborates the concentration–time interplay observed in the TOC removal data. The degradation process follows pseudo-first-order kinetics across all tested TOC concentrations, with R^2 values ranging from 0.9292 to 0.9590. The k demonstrated a progressive decrease with increasing initial CIP concentration: 0.0665 min^{-1} ($R^2 = 0.9590$) at 3 mg L^{-1} (TOC), 0.0623 min^{-1} ($R^2 = 0.9466$) at 6 mg L^{-1}, 0.0532 min^{-1} ($R^2 = 0.9484$) at 12 mg L^{-1}, 0.0384 min^{-1} ($R^2 = 0.9406$) at 24 mg L^{-1} and 0.0354 min^{-1} ($R^2 = 0.9292$) at 36 mg L^{-1}. The declining values of k manifest as shallower slopes in the semi-logarithmic plots, particularly pronounced in the initial phases (15–25 min), where the steepest declines occur at lower concentrations. This indicates that higher concentrations of CIP impose constraints on kinetic rates, as ROS generation struggles to keep pace with the influx of pollutants.[52]

Casually, the observed reliance on the initial CIP concentration stems from the catalytic system's finite capacity to produce and utilize ROS effectively. At low TOC concentrations (3–6 mg L^{-1}), the abundance of ozone-derived ROS (*e.g.*, $^{\bullet}OH$ and $O_2^{\bullet-}$) relative to the number of pollutant molecules enables efficient, non-selective oxidation, facilitating rapid cleavage of CIP's quinolone and piperazine moieties and promoting comprehensive mineralization of intermediates. As supported by high k values and near-complete TOC removals, the GO@ZnO@MnO_2 catalyst architecture further enhances this process by promoting ozone activation through surface hydroxyl groups and oxygen vacancies in ZnO, complemented by redox activities of Mn(IV)/Mn(III),[53] ensuring sufficient interfacial reactions throughout the duration of the study. Conversely, at higher TOC concentrations (24–36 mg L^{-1}), the increased pollutant load results in competition for active sites and ROS generation, leading to catalyst surface saturation. This saturation results in partial oxidation rather than complete mineralization and can lead to the accumulation of recalcitrant byproducts that scavenging radicals, further diminishing the overall efficacy of the system. Consequently, this results in reduced k values and overall efficiencies, with extended reaction times failing to fully counter these limitations due to mass transfer constraints and potential inhibitory effects from the organic overload present.[54]

Therefore, the performance of the O_3/GO@ZnO@MnO_2 system is inversely affected by the initial CIP concentration, with optimal mineralization (94.97% TOC removal at 50 min and $k = 0.0665$ min^{-1}, $R^2 = 0.9590$) observed at 3 mg L^{-1}. However, practical applications may target moderate concentrations, such as 12 mg L^{-1}, where 90.20% removal is achievable with $k = 0.0532$ min^{-1} ($R^2 = 0.9484$). These findings highlight the need to consider influent concentration when designing processes, potentially using dilution or multi-stage treatment strategies to maintain high efficiency in real-world antibiotic wastewater remediation efforts.

Machine learning model for removal prediction

The ML models were developed to describe the influence of operating parameters on TOC removal within the optimized O_3/GO@ZnO@MnO_2 (60 : 35 : 5) catalytic ozonation system. Because catalyst composition was not included as an input feature, the present ML analysis should be interpreted as process-condition modeling rather than catalyst-composition or structure–performance modelling. Building upon the comprehensive evaluation of operational parameters, including pH, catalyst dosage, reaction time and initial CIP concentration, which collectively influence the catalytic ozonation process, machine learning (ML) models were developed to predict TOC removal efficiency in the O_3/GO@ZnO@MnO_2 (60 : 35 : 5) system. Four ML algorithms – Linear Regression (LR), Artificial Neural Network (ANN), Random Forest (RF) and Support Vector Machine (SVM) – were trained and tested using a dataset comprising 160 samples, with input features including pH, reaction time, catalyst dosage and initial CIP concentration (corresponding to TOC levels) and the target variable being TOC removal efficiency (%). The dataset was partitioned into 80% training (128 samples) and 20% testing (32 samples), with hyperparameter optimization *via* grid or random search to enhance model precision, as detailed in the methodology.

Model performance was evaluated using the coefficient of determination (R^2), root mean square error (RMSE), and mean absolute error (MAE) to assess how well each algorithm represented the nonlinear response patterns in the available experimental dataset. Because the observations were derived from time-resolved batch experiments, these metrics should be interpreted as indicators of predictive fit within the investigated domain rather than as definitive evidence of strict trajectory-level generalization. As illustrated in Fig. 9, the ANN model provided the strongest predictive fit within the available dataset, with an R^2 of 0.977, RMSE of 4.26 and MAE of 2.717 on the testing subset. However, because the dataset contained only 160 time-resolved observations, the ANN result should be interpreted cautiously. Although the test-set performance suggests that severe underfitting did not occur, the possibility of optimistic performance due to limited sample size and temporal dependence cannot be excluded.[55] The RF model performed admirably, with an R^2 of 0.946, RMSE of 6.844, and MAE of 5.39, leveraging ensemble learning to capture complex interactions among the inputs. In contrast, the LR model (Fig. 9b) yielded the lowest performance (R^2 = 0.686, RMSE = 15.721, MAE = 12.418), underscoring its limitations in handling non-linear relationships inherent in catalytic ozonation processes.[56]

Comparing algorithms also provides useful information about possible underfitting and overfitting. The relatively low LR performance ($R^2 = 0.686$) suggests that a purely linear model may underfit the nonlinear response patterns observed in catalytic ozonation. In contrast, ANN and SVM achieved much higher fitting performance, indicating their ability to capture nonlinear relationships among reaction time, pH, catalyst dosage and initial CIP concentration. Nevertheless, because flexible nonlinear models can overfit small datasets, their high R^2 values should be regarded as evidence of strong fit within the present dataset rather than definitive proof of generalization. RF showed intermediate performance, suggesting a trade-off between nonlinear fitting capacity and robustness to noise.

These metrics indicate that ANN and SVM provided the strongest predictive fit among the tested algorithms within the current dataset. The close clustering of predicted and observed values around the 1 : 1 line suggests that these models captured the nonlinear relationship between reaction time, operating conditions, and TOC removal in the studied experimental domain. However, because temporally correlated observations from the same reaction trajectory may be represented in both training and testing subsets, these results should not be interpreted as conclusive evidence of robust extrapolation to fully independent batch experiments. To elucidate the relative contributions of input variables to the predictions, feature importance analyses were conducted for each model, as depicted in Fig. 10 through bar plots. Across all models, this confirms that the model captured the kinetic progression of TOC abatement during CIP degradation under the studied operating conditions, but it should not be interpreted as a new mechanistic discovery.

Catalyst dosage (Cat_dos) ranked second in importance (scores of 8–12), aligning with its impact on active-site availability and interfacial reactions. Solution pH (pH) was assigned a moderate importance (scores 3–6), consistent with its modulation of ozone decomposition and catalyst surface chemistry. Initial TOC concentration (CIP_con) consistently showed the lowest importance (scores < 3), suggesting that, while it affects overall efficiency, its predictive weight is subordinate to time-dependent and catalytic factors within the modeled range.[57]

Computational efficiency was also considered to assess practical applicability, with processing times measured on a standard system (8 GB RAM, Intel Core i3-10105 CPU at 3.70 GHz). The LR model required negligible time (<0.1 seconds), making it suitable for rapid prototyping despite lower accuracy. The ANN, with grid search over hidden layers, took 4.07 seconds; RF tuning and training totaled 16.90 seconds; and SVM optimization consumed 11.97 seconds. These costs indicate a trade-off between model complexity and runtime, favoring ANN and SVM for high-fidelity predictions in resource-constrained environmental modeling scenarios. Therefore, the ML framework should be viewed as a preliminary data-driven representation of TOC degradation behaviour in the O_3/GO@ZnO@MnO_2 system. Within the available dataset, ANN and SVM provided the best fits among the tested models, and reaction time emerged as the most influential predictor, consistent with the process's kinetic nature. Nevertheless, due to the time-resolved structure of the dataset, the present ML results should be interpreted as exploratory response modeling rather than as a definitive benchmark for predicting fully independent reaction trajectories or scale-up scenarios.

The high importance of reaction time is chemically reasonable because catalytic ozonation is a kinetic process in which TOC removal evolves progressively with ozone exposure, catalyst-mediated ozone activation and accumulation of reactive oxidizing species. However, the strong contribution of reaction time may also partly reflect the dataset's time-profile

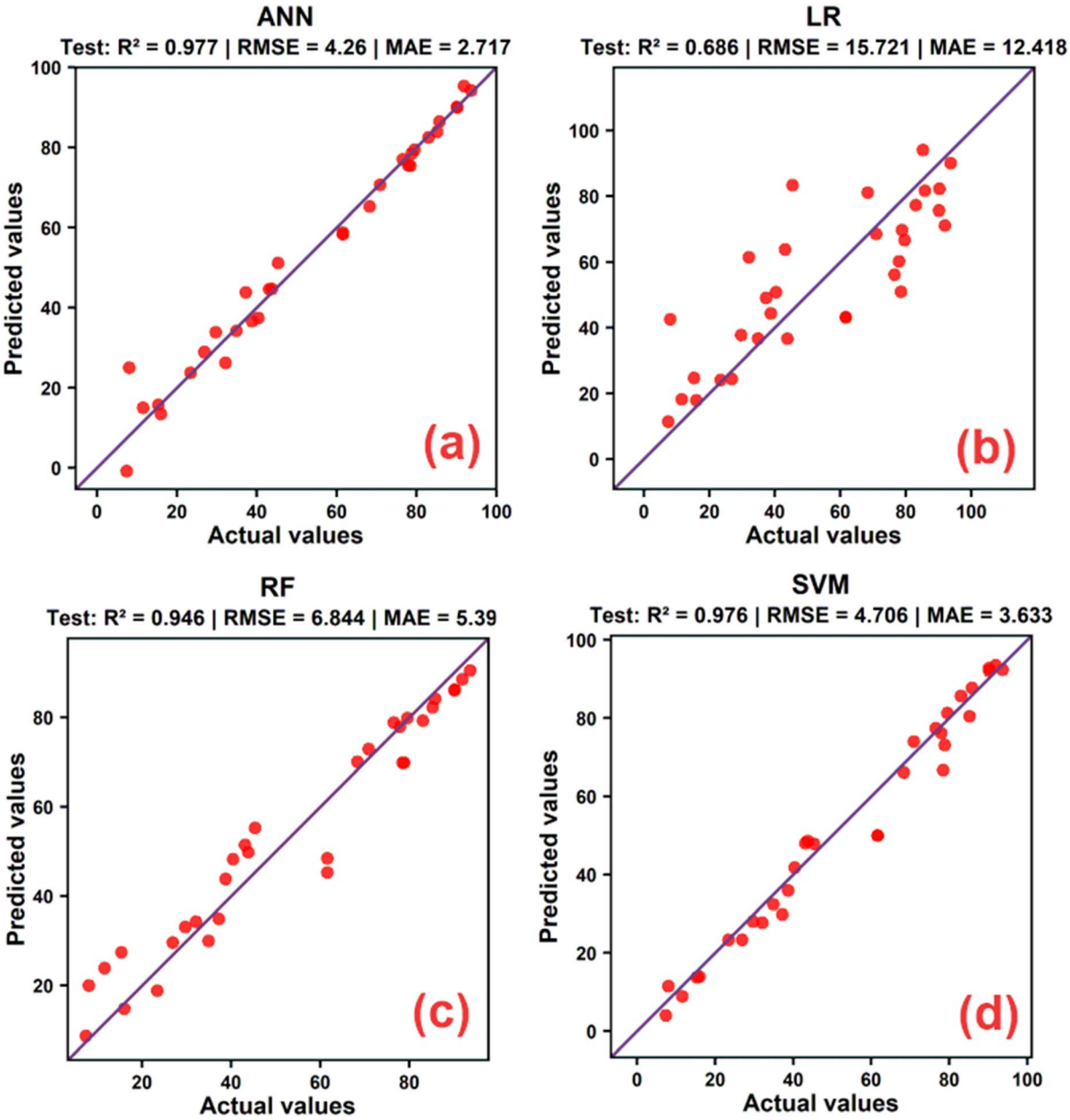

Fig. 9 The prediction of ML models: ANN (a); LR (b); RF (c); SVM (d) for TOC abatement efficiency during CIP degradation by O_3/GO@ZnO@MnO_2 system.

structure. Therefore, the variable-importance results should be interpreted as mechanistically informative within the present experimental design, rather than as evidence of model transferability beyond the measured kinetic domain.

In real wastewater, natural organic matter, humic substances, carbonate/bicarbonate alkalinity, chloride, sulfate, nitrate, ammonia, suspended solids and background COD/TOC may compete with CIP for oxidizing species, scavenge radicals, alter ozone decomposition, or modify catalyst surface interactions. Therefore, matrix descriptors should be incorporated into future ML datasets to improve practical applicability.

To provide a more robust interpretation of model behavior, SHAP analysis was further performed, and the resulting summary plot is shown in Fig. 11. Unlike conventional feature-importance ranking, SHAP analysis provides both the relative importance of each variable and the direction of its contribution to individual predictions. The SHAP plot shows that reaction time had the widest distribution of SHAP values, ranging from strongly negative to strongly positive contributions, confirming it was the most influential input variable in predicting TOC removal. Low reaction-time values were associated with negative SHAP values, whereas high reaction-time values were associated with positive SHAP values. This trend is chemically reasonable because longer reaction times increase ozone exposure and enhance the cumulative oxidative transformation of CIP and its intermediates. It should be emphasized that

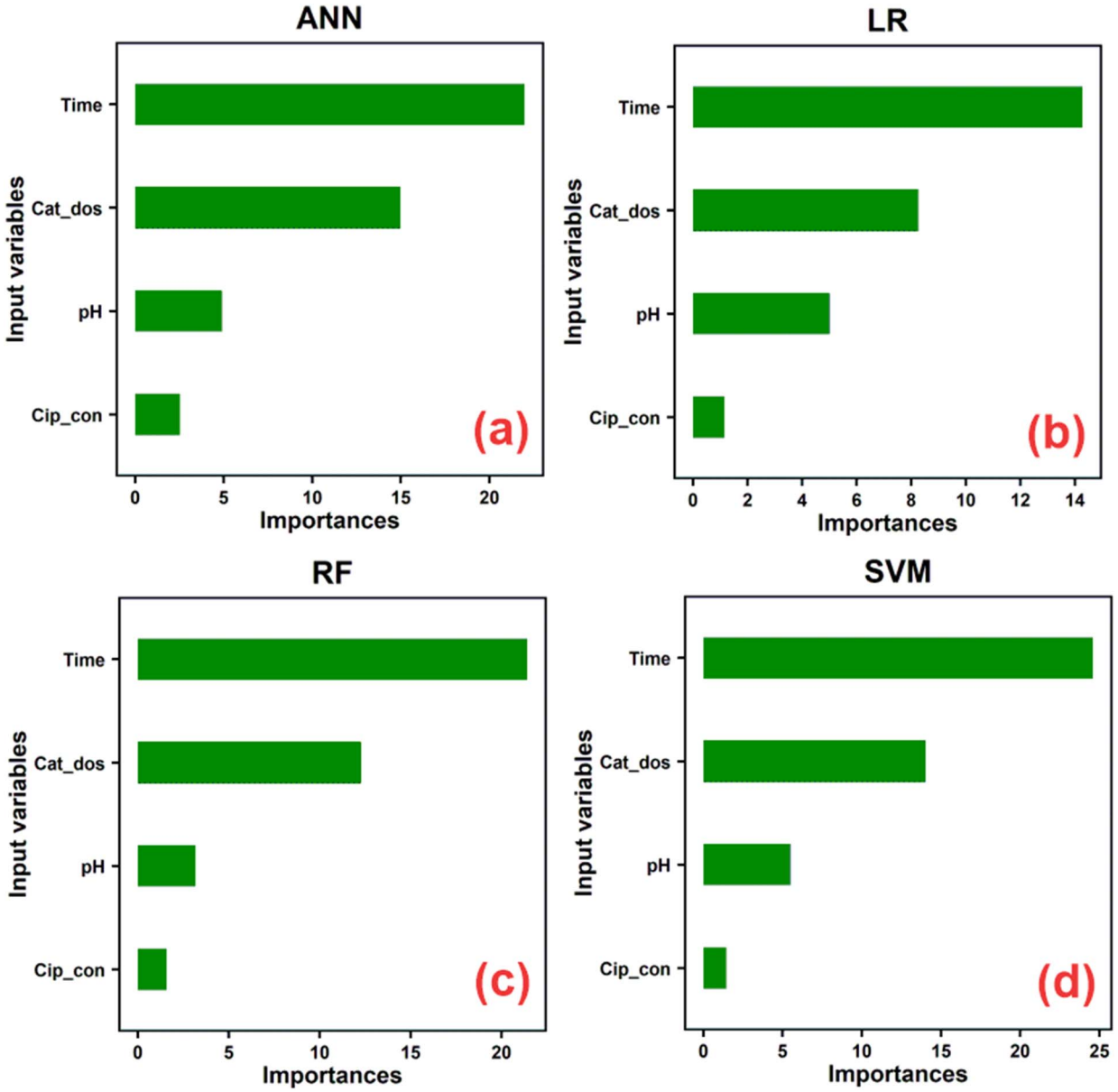

Fig. 10 Importance plot of ML models: ANN (a); LR (b); RF (c); SVM (d) for TOC degradation efficiency by O_3/GO@ZnO@MnO_2 system.

reaction time was included as an operational/time-index variable and should not be interpreted as an independent mechanistic factor or intrinsic reaction-rate descriptor; rather, its high SHAP contribution indicates that the model captured the expected temporal progression of TOC abatement in the batch system.

Catalyst dosage was the second-most-influential variable. Higher catalyst dosages generally yielded positive SHAP values, indicating that increasing GO@ZnO@MnO_2 dosage promoted TOC removal, likely by providing more active sites for ozone activation and interfacial oxidation. Conversely, lower catalyst dosages tended to degrade model predictions, reflecting insufficient active-site availability at low catalyst levels.

The SHAP distribution for pH indicates a moderate but clear contribution to model output. Higher pH values were mainly associated with positive SHAP values, consistent with enhanced ozone decomposition and increased formation of reactive oxidizing species under alkaline conditions. Lower pH values generally had a negative effect, suggesting less favorable ozone activation and slower mineralization under acidic conditions.

Initial TOC concentration showed the smallest overall SHAP contribution among the four variables. High TOC concentrations tended to yield positive SHAP values in some regions of the dataset, whereas low concentrations were distributed closer to zero or negative SHAP values. This behavior suggests that the effect of pollutant loading on TOC removal is nonlinear and may interact with reaction time and catalyst dosage. At higher pollutant concentration, the absolute TOC removal response may increase within the studied range, although excessive loading can still reduce apparent removal efficiency due to competition for reactive oxidizing species.

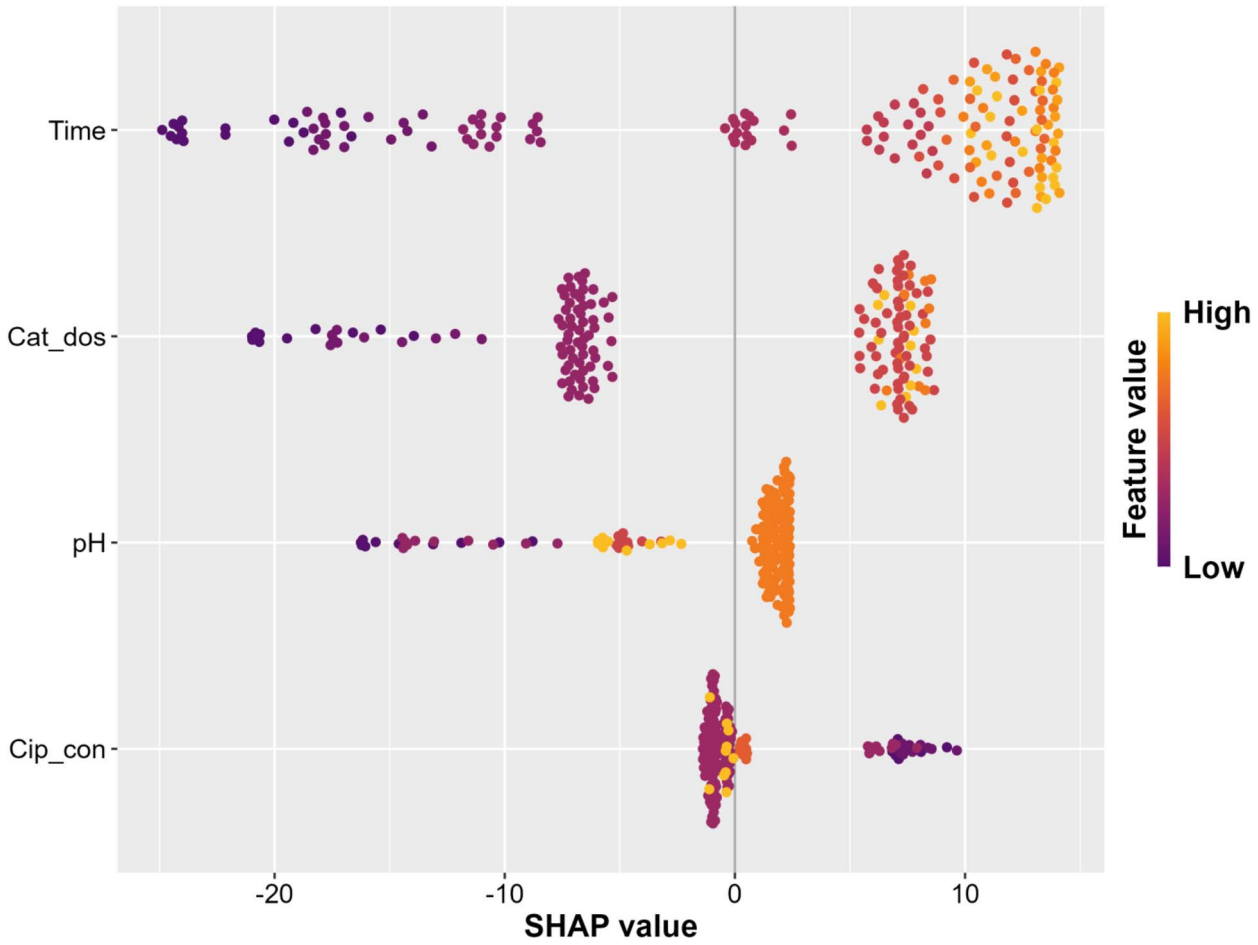

Fig. 11 SHAP summary plot explaining the contribution of operating variables to the ML-predicted TOC removal during CIP degradation in the O_3/GO@ZnO@MnO_2 system.

Overall, the assessment of overfitting remains limited because only an 80 : 20 split was used in the present study. More rigorous diagnostics, including learning curves, repeated cross-validation, grouped/block validation by independent reaction trajectories, and external validation with newly generated experiments, are required to distinguish overfitting from true predictive generalization more clearly. Accordingly, the ANN model is retained as a comparative nonlinear modeling approach, but its performance should be interpreted as preliminary.

Mechanism of ciprofloxacin degradation in the O_3/GO@ZnO@MnO_2 system

The present results suggest a possible interfacial charge-transfer-assisted pathway; however, the available experimental evidence is insufficient to definitively confirm a Z-scheme mechanism. Based on the kinetic behavior, scavenger experiments and catalyst characterization results, the oxidation mechanism in the O_3/GO@ZnO@MnO_2 (60 : 35 : 5) system was re-evaluated more cautiously. The available evidence indicates that hydroxyl-radical-related oxidation contributes significantly to CIP mineralization; however, the incomplete inhibition observed in the presence of scavengers suggests that the process does not rely exclusively on free dissolved $^{\bullet}OH$. Instead, the overall catalytic ozonation likely involves multiple concurrent pathways, including aqueous radical oxidation, surface-mediated reactive oxygen species generated on the catalyst interface, and direct ozone attack on susceptible moieties of CIP.[41,58] In addition, because GO is a major component of the nanocomposite, adsorption may facilitate overall removal by concentrating ciprofloxacin and its transformation products near catalytically active sites. However, since no adsorption-only control experiment was conducted in the absence of ozone, the extent of this adsorption contribution could not be quantified separately from oxidative removal in the present study.

The radical-interference experiments were conducted in the O_3/GO@ZnO@MnO_2 system under the optimized conditions: initial TOC concentration of 12.21 mg L^{-1}, pH 9.0, catalyst dosage of 1.00 g L^{-1}, and reaction time of 0–50 min. Radical-interference tests were conducted using carbonate ions (CO_3^{2-}) and chloride ions (Cl^-) to assess the possible contribution of $^{\bullet}OH$-related radical pathways to TOC abatement during CIP degradation, as shown in Fig. 12. Because these ions may also affect catalyst surface reactions, ozone activation, or oxidation of TOC-containing intermediates, their inhibitory effects were interpreted cautiously as evidence for the participation of radical-mediated oxidation rather than direct proof of

an exclusively ˙OH-controlled mechanism. CO_3^{2-} selectively quenches ˙OH with a high rate constant ($k = 3.9 \times 10^8$ M^{-1} s^{-1}), forming the less oxidative carbonate radical ($^{\cdot}CO_3^-$, $E^0 = 1.78$ V *vs.* SHE), while Cl^- reacts rapidly with ˙OH ($k = 4.3 \times 10^9$ M^{-1} s^{-1}) to generate chlorine radicals ($Cl^{\cdot}$, $E^0 \approx 2.4$ V) or hypochlorite, which may offer secondary oxidation but typically reduces overall efficiency due to lower selectivity.[59,60] In the control system (no scavengers), the normalized TOC concentration (C_t/C_0) declined sharply from 1.000 at $t = 0$ to 0.098 at $t =$ 50 min, achieving 90.2% removal. Linear regression fitting of $\ln(C_t/C_0)$ *versus* time ($t > 0$) yielded the k of 0.0526 min^{-1} with $R^2 = 0.9313$, confirming adherence to first-order kinetics and rapid initial degradation (*e.g.*, $C_t/C_0 = 0.651$ at $t = 10$ min, corresponding to 34.9% removal). The addition of CO_3^{2-} markedly suppressed this, resulting in a final C_t/C_0 of 0.175 (82.5% removal) and a reduced k of 0.0411 min^{-1} ($R^2 = 0.9367$), representing a 21.9% decrease in k. Similarly, Cl^- yielded $C_t/C_0 =$ 0.158 (84.2% removal) and $k = 0.0408$ min^{-1} ($R^2 = 0.9357$), a 22.4% k reduction. The observed decreases in the pseudo-first-order rate constant (21.9–22.4%) and the moderate reduction in final TOC removal demonstrate that hydroxyl radical-related oxidation is involved in the mineralization process. Nevertheless, the fact that substantial catalytic activity was retained after scavenger addition indicates that free aqueous ˙OH cannot be considered the sole oxidation pathway under the present conditions. Rather, these results are more consistent with a mixed mechanism in which interfacial oxidation routes – such as catalyst-surface ROS, adsorbed active oxygen species, and/or direct ozone reactions – also contribute appreciably to CIP degradation.[61,62] As shown in Fig. 12, the presence of CO_3^{2-} and Cl^- reduced both the final TOC removal and the apparent pseudo-first-order rate constant for TOC abatement. The decrease in k_d indicates that radical-mediated oxidation contributed to overall mineralization. Nevertheless, the inhibition was only partial, and substantial TOC removal persisted after the addition of these ions. Therefore, the scavenger/interference results do not support a mechanism controlled exclusively by free aqueous ˙OH. Instead, they are more consistent with a mixed oxidation pathway involving ˙OH-related oxidation, surface-mediated ozone activation, adsorbed reactive oxygen species, and direct ozone reactions. Because CO_3^{2-} and Cl^- can also interact with catalyst surfaces and TOC-containing intermediates, the observed inhibition should be interpreted cautiously and should not be assigned solely to homogeneous ˙OH scavenging. Therefore, the scavenger/interference results should be interpreted as evidence for the participation of radical-mediated pathways, rather than as definitive proof that free aqueous ˙OH is the dominant or exclusive oxidizing species.

Material characterizations substantiate this ˙OH dominance, elucidating the catalyst's role in ozone activation. SEM images revealed a porous morphology with MnO_2 and ZnO nanoparticles (20–50 nm) uniformly anchored on GO sheets, enhancing surface area (likely >200 m^2 g^{-1} based on similar nanocomposites) and exposing abundant active sites, as confirmed by XRD peaks for hexagonal ZnO (wurtzite phase) and tetragonal MnO_2 (α-phase), alongside GO's amorphous carbon. EDX results showed elemental ratios approximating 60 : 35 : 5 (GO : ZnO : MnO_2), with oxygen content indicating vacancies (O/Zn ≈ 0.9–1.0, typical for defective ZnO). These vacancies trap electrons, while MnO_2's variable oxidation states enable redox cycling ($Mn^{4+} \leftrightarrow Mn^{3+}$, $E^0 \approx 1.51$ V), synergistically promoting O_3 decomposition. Under optimal conditions (pH 9, 1.0 g per L dosage, 12.21 mg per L TOC), alkaline OH^- initiates homogeneous O_3 decay:

$$O_3 + OH^- \rightarrow HO_2^- + O_2,\ k = 70\ M^{-1}\ s^{-1};\ HO_2^- + O_3 \rightarrow {}^{\cdot}OH + O_2^{\cdot -} + O_2,\ k = 2.8 \times 10^6\ M^{-1}\ s^{-1},$$

Amplified heterogeneously on the catalyst surface. Specifically, O_3 adsorbs onto Mn^{4+} sites:

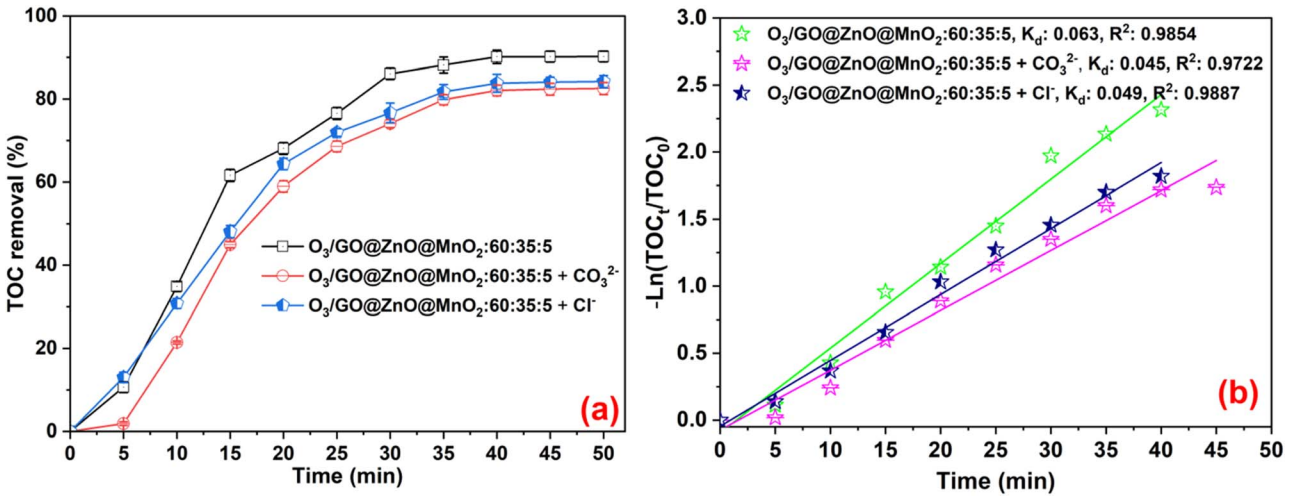

Fig. 12 Influence of scavengers (CO_3^{2-} and Cl^-) on removal of CIP (a) TOC and (b) pseudo-first-order rate constants for TOC abatement during CIP degradation by O_3/O_3/GO@ZnO@MnO_2 system at initial TOC concentration of 12.21 mg L^{-1}; pH of 9.0; catalyst dosage of 1.00 g L^{-1} and contact time of 0–50 min.

$$Mn^{4+} + O_3 + e^- \rightarrow Mn^{3+} + {}^{\bullet}O_3^-,$$

Followed by ${}^{\bullet}O_3^-$ protonation:

$${}^{\bullet}O_3^- + H^+ \rightarrow {}^{\bullet}OH + O_2,\ k \approx 10^9\ M^{-1}\ s^{-1}.$$

ZnO's oxygen vacancies facilitate electron donation, and GO's π–electron system acts as a mediator for charge transfer, preventing recombination and sustaining ROS production. This is evidenced by the pH 9 peak k of 0.039 min^{-1} (from earlier studies), where CIP's zwitterionic form ($pK_{a1} = 6.09$, $pK_{a2} = 8.62$) enhances electrostatic adsorption onto the catalyst, boosting surface reactions. At a 1.0 g per L dosage, the maximal site yield k = 0.0532 min^{-1}, while higher concentrations (*e.g.*, 2.0 g L^{-1}, k = 0.0463 min^{-1}) induce aggregation, reducing effective area and ROS yield, consistent with ML's dosage importance (8–12 units).

A possible interpretation of the synergistic catalytic behavior is that the GO support facilitates interfacial electron transfer among ZnO, MnO_2 and adsorbed ozone species, thereby promoting ozone activation and reactive oxygen species generation at the catalyst surface. However, based on the present evidence, this pathway should be regarded as a plausible mechanistic hypothesis rather than a single definitive route. Although the Mn(IV)/Mn(III) redox cycling and oxygen vacancies can theoretically generate superoxide radicals ($O_2^{\bullet-}$) *via* one-electron reduction of ozone, the contribution of $O_2^{\bullet-}$ was not directly verified in the present study because a specific superoxide scavenger (*e.g.*, *p*-benzoquinone) was not employed. Consequently, the role of superoxide remains speculative. Therefore, the proposed interfacial mechanism should be regarded as a plausible mechanistic hypothesis rather than a definitively proven pathway. Further validation using DFT calculations, EPR spin-trapping, and *in situ* spectroscopic techniques would be necessary to directly identify ozone adsorption sites, interfacial charge-transfer routes, and ROS-generation steps.

This aligns with the existing literature, which indicates similar pathways in the degradation of pharmaceutical contaminants, confirming that effective catalysis arises from these interconnected reaction mechanisms.[63,64] Previous studies on ciprofloxacin and structurally related fluoroquinolones in other advanced oxidation systems have reported transformation patterns involving oxidation of the quinolone core and piperazine-containing moieties. These reports provide useful contextual support for interpreting possible reaction tendencies; however, such pathways should not be considered directly verified for the present O_3/GO@ZnO@MnO_2 system without dedicated intermediate identification.[65] The work of Luo *et al.* (2023)[66] emphasized the effectiveness of GO@MnO_2 in ozonating 4-nitrophenol, achieving substantial yields *via* surface-bound (OH) intermediates, with kinetics enhancements up to five-fold over ozone alone, which resonates with the findings on CIP degradation. Further, photocatalytic systems such as GO@ZnO@Ag for CIP illustrate similar electron transfer dynamics, with efficiencies exceeding 95% attributed to the synergetic effects of silver nanoparticles, akin to those realized here with MnO_2 and ZnO.[67]

Proposed transformation intermediate pathways of CIP: from the possible chemical structures of the intermediates generated during CIP degradation, several plausible degradation pathways can be proposed for CIP in the O_3/GO@ZnO@MnO_2 catalytic ozonation system, as illustrated in Fig. 13. The parent CIP molecule, assigned as $C_{17}H_{18}FN_3O_3$ with [M + H]+ at m/z 332.1, contains several reactive sites, including the piperazine moiety at C7, the fluorine substituent at C6, the carboxylic group at C3 and the quinolone aromatic core. These sites are susceptible to attack by hydroxyl radical-related oxidants, surface-bound reactive oxygen species, and direct ozone-derived oxidation pathways. Pathway A can be attributed to piperazine-ring cleavage. In this route, partial cleavage of the piperazine side chain produces A1 ($C_{15}H_{13}FN_2O_3$, m/z 289.1), followed by further loss of amine-containing side-chain fragments to form A2 ($C_{13}H_{10}FNO_3$, m/z 248.1). Subsequent ring contraction and fragmentation generate A3 ($C_{11}H_8FNO_3$, m/z 222.1), while deeper oxidative cleavage produces the smaller aromatic acid fragment A4 ($C_8H_6O_4$, m/z 167.0). This pathway is chemically reasonable because the piperazine ring is electron-rich and is commonly reported as a preferred site of attack during the oxidative degradation of fluoroquinolone antibiotics. The final products of this route may include small organic acids such as oxalic acid, formic acid, and acetic acid, which may undergo partial or complete mineralization depending on reaction time and oxidant availability. Pathway B corresponds to defluorination followed by decarboxylation and side-chain fragmentation. The first step involves loss of fluorine from the parent CIP structure, yielding B1 ($C_{17}H_{19}N_3O_3$, m/z 314.1). Further transformation, *via* the loss of small side-chain fragments and decarboxylation, produces B2 ($C_{16}H_{19}N_3O_2$, m/z 286.1). Cleavage of C–N bonds and removal of F-containing or amine-containing fragments can then generate B3 ($C_{12}H_{12}NO_2$, m/z 200.1). This route indicates that the C6–F bond and the piperazine-containing side chain are both involved in the oxidative transformation of CIP. The released fluorine may ultimately exist as inorganic fluoride, whereas the remaining organic fragments may continue to oxidize into low-molecular-weight acids or persistent aromatic residues. Pathway C involves quinolone-core hydroxylation accompanied by decarboxylation and subsequent fragmentation. The intermediate C1 ($C_{16}H_{18}FN_3O_3$, m/z 320.1) can be assigned to a hydroxylated/decarboxylated CIP derivative, indicating that oxygen incorporation and CO_2 loss may occur in a coupled transformation step. Further cleavage of the piperazine side chain generates C2 ($C_{13}H_{10}FNO_3$, m/z 248.1), followed by ring opening to form C3 ($C_{10}H_8FNO_3$, m/z 210.1). Subsequent fragmentation can produce C4 ($C_7H_6O_4$, m/z 155.0), which may be further oxidized to small carboxylic acids. This pathway suggests that hydroxylation of the quinolone core weakens the aromatic framework and promotes progressive ring fragmentation. Pathway D represents direct decarboxylation of the parent CIP molecule, involving the loss of CO_2 from the C3 carboxylic group. This route may proceed in parallel with Pathways A–C and generate lower-molecular-weight quinolone fragments, followed by

piperazine cleavage, aromatic-ring fragmentation and formation of small organic acids or persistent aromatic fragments. Importantly, not all transformation routes necessarily lead to complete mineralization to CO_2 and H_2O within the investigated reaction time. Instead, the degradation process may involve the coexistence of mineralization and accumulation of lower-molecular-weight transformation products.

In addition to evaluating operational reusability based on TOC removal, the chemical stability of GO@ZnO@MnO_2 was further assessed by ICP-OES analysis of Zn and Mn leaching in the treated solution. After catalytic ozonation under the optimized conditions, the dissolved Zn and Mn concentrations were only 0.00025 and 0.00018 mg L^{-1}, respectively. These extremely low concentrations indicate negligible metal release from the composite during the oxidation process and suggest that the ZnO and MnO_2 phases were effectively stabilized within the GO-supported heterostructure.

The very low Zn and Mn leaching levels can be attributed to the relatively stable oxide nature of ZnO and MnO_2 and their immobilization on the GO matrix. The oxygen-containing functional groups and large interfacial area of GO may contribute to anchoring ZnO and MnO_2 nanoparticles, thereby reducing particle detachment and metal dissolution. In addition, MnO_2 is a high-valence manganese oxide and is relatively stable under the oxidative ozonation environment, which does not favor extensive reduction of Mn(IV) to soluble Mn^{2+} in the

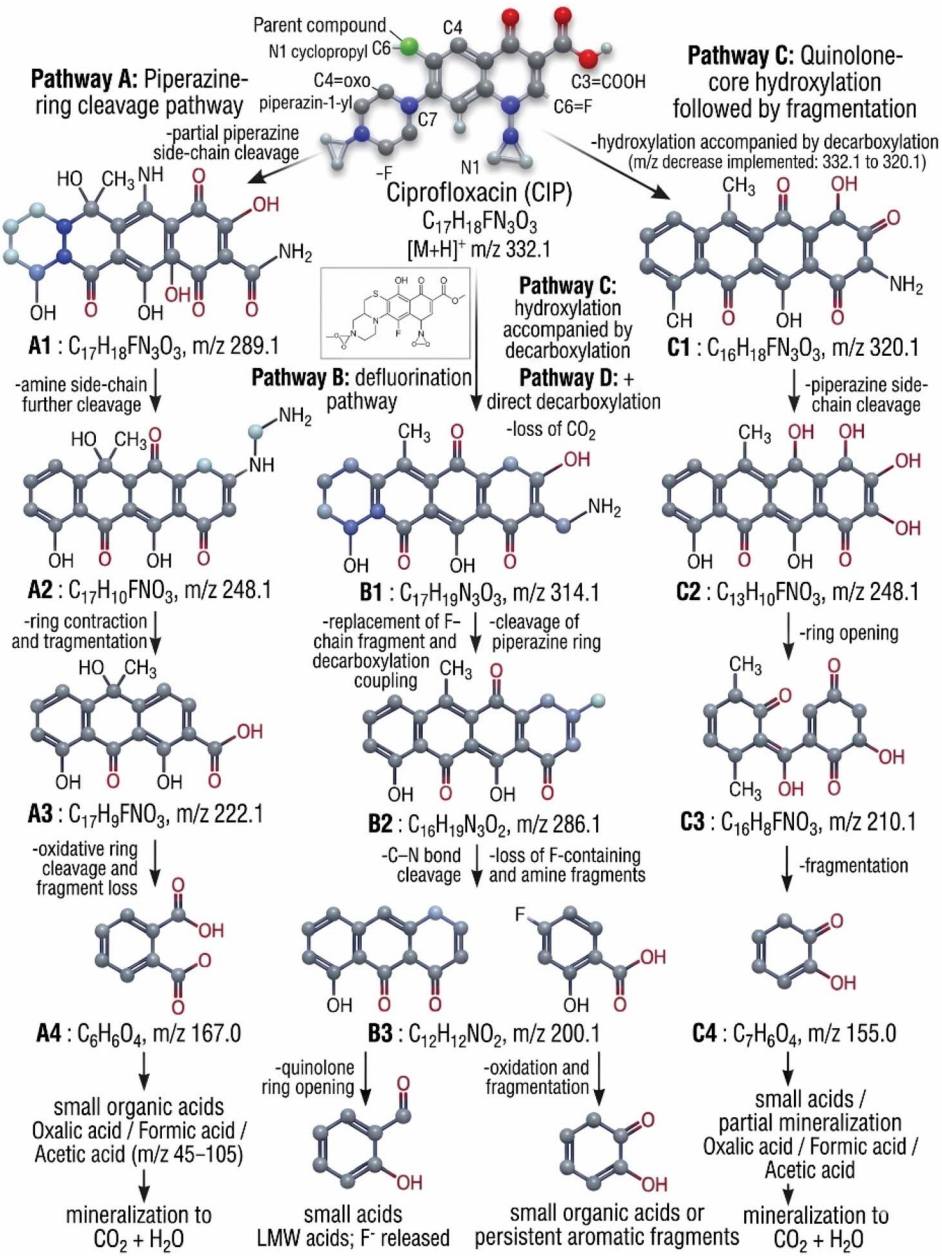

Fig. 13 Proposed transformation intermediate pathways of ciprofloxacin during catalytic ozonation over GO@ZnO@MnO_2.

absence of strong reductants. The retained catalytic activity during reuse, together with the ICP-OES results, supports the good chemical stability of the GO@ZnO@MnO_2 composite under the tested laboratory conditions. These findings indicate that the risk of secondary Zn or Mn contamination from the catalyst was very low in the present system. Nevertheless, longer-term continuous operation and leaching tests under real wastewater matrices and broader pH ranges would still be necessary before practical application.

The present study provides a controlled laboratory-scale evaluation of CIP degradation by O_3/GO@ZnO@MnO_2 using synthetic CIP-contaminated water. This design enabled the intrinsic catalytic activity of the nanocomposite and the effects of pH, reaction time, pollutant concentration and catalyst dosage to be evaluated without matrix interference. However, the practical application of this system to real wastewater requires further validation. Real wastewater contains natural organic matter, humic substances, carbonate/bicarbonate alkalinity, chloride, sulfate, nitrate, ammonia, suspended solids and other coexisting contaminants, which may compete for reactive oxidizing species, inhibit ozone decomposition, occupy catalyst active sites, or alter interfacial oxidation pathways. Therefore, the current results should be considered a proof-of-concept and mechanistic baseline rather than a complete field-scale validation. Future work should evaluate the process in real wastewater and matrix-spiked synthetic wastewater and should develop matrix-aware ML models that include wastewater-quality descriptors such as COD, TOC background, alkalinity, conductivity, major anion concentrations, humic acid content, turbidity and coexisting micropollutants.

Although the current experimental results support enhanced catalytic ozonation by the GO@ZnO@MnO_2 composite, the exact elementary mechanism remains unresolved. Computational analysis, particularly DFT modelling, could help determine ozone adsorption energies, charge redistribution at GO/ZnO/MnO_2 interfaces, oxygen-vacancy effects, and the thermodynamic feasibility of ROS formation. Such analysis, combined with additional experimental validation, should be pursued in future work to confirm the proposed mechanism more rigorously.

Conclusions

A highly active and stable ternary GO@ZnO@MnO_2 (60 : 35 : 5) nanocomposite was synthesized *via* a simple, eco-friendly one-step electrochemical exfoliation route and demonstrated exceptional catalytic ozonation performance for ciprofloxacin. Under optimized conditions (pH 9.0, 1.0 g L^{-1} catalyst dosage), the system achieved 90.20% TOC removal within 50 min, corresponding to a pseudo-first-order rate constant of 0.0532 min^{-1} – markedly superior to single ozonation (32.52%, $k = 0.010$ min^{-1}) and binary GO@ZnO systems. Comprehensive characterization (SEM, XRD and EDX) revealed that the superior activity originated from the well-dispersed heterostructure, abundant oxygen vacancies, and synergistic Mn(IV)/Mn(III) redox cycling facilitated by the conductive GO platform.

Scavenger experiments showed that hydroxyl-radical-mediated oxidation contributed to the mineralization process, although the partial inhibition observed after addition of CO_3^{2-} and Cl^- indicates that other pathways, including surface-mediated ozone activation and direct oxidation routes, also participated. Because catalyst-only adsorption equilibrium experiments were not performed, the separate contribution of physical adsorption by the GO-containing nanocomposite could not be quantified explicitly and should be clarified in future ozone-free control studies.

The catalyst maintained high activity over five reuse cycles, highlighting its practical durability. Integration of machine-learning models further strengthened the study. Among the four algorithms evaluated, ANN and SVM showed the strongest fitting performance within the available dataset, suggesting that nonlinear models can better describe the experimental response patterns than linear regression. However, given the limited dataset size and time-resolved data structure, the possibility of overfitting cannot be excluded, and future work should include learning-curve analysis, grouped cross-validation and external validation. These models provide a preliminary data-driven tool for describing the experimental response behaviour and supporting interpretation of the relative influence of operating variables within the studied domain. However, because the ML dataset was derived from time-resolved batch reaction profiles, the reported model performance may be affected by temporal autocorrelation and should therefore be interpreted with caution.

SHAP analysis was further incorporated to improve model interpretability. The SHAP results showed that reaction time had the largest contribution to predicted TOC removal, reflecting its role as an operational time-index variable in the batch degradation dataset rather than an independent mechanistic rate descriptor. However, because catalyst descriptors were not included in the ML input space, the SHAP analysis should be interpreted as process-variable explainability within the optimized catalyst system rather than as structure–performance modelling. The proposed CIP transformation pathway, based on possible intermediate structures and assigned m/z values, suggests that degradation proceeds through multiple concurrent routes, including piperazine-ring cleavage, defluorination/decarboxylation, quinolone-core hydroxylation, and direct decarboxylation. These routes progressively generate lower-molecular-weight intermediates and small organic acids, although complete mineralization may not occur along all pathways within the investigated reaction time. Further MS/MS-based structural confirmation would be valuable to verify individual intermediates and distinguish possible isomeric products.

This work represents a significant advancement in antibiotic wastewater treatment by combining green catalyst synthesis, high mineralization efficiency, good operational reusability and reliable machine-learning prediction within a single framework. The developed GO@ZnO@MnO_2 nanocomposite and associated ML approach offer a scalable, cost-effective, and environmentally benign solution for the removal of recalcitrant fluoroquinolones. Future research will focus on pilot-scale validation, real wastewater matrix effects, and further refinement of interpretable ML models to accelerate the translation of

catalytic ozonation technology into practical applications. The findings of this study provide valuable insights toward achieving sustainable, efficient remediation of emerging pharmaceutical contaminants in water resources. Because the present ROS analysis relied primarily on scavenger experiments, further mechanistic confirmation by EPR spin-trapping, selective quenchers for other ROS species, and surface-sensitive spectroscopic techniques would be valuable in future studies to distinguish more conclusively between aqueous and interfacial oxidation pathways.

Author contributions

Le Phuong Hoang: funding acquisition, investigation; Thi Hong Vien Nguyen, Thi Dong Nguyen, Thi Hong Huyen Chu, Thu Huyen Nguyen: conceptualization, data curation; Van-Truong Nguyen, Vu Thi Thuy Trang, Van-Truong Nguyen: formal analysis; Van-Truong Nguyen, Huu-Tap Van: resources, software; Thi Minh Phuong Nguyen, Huu-Tap Van: writing – original draft; Huu-Tap Van: methodology; Van Hung Hoang, Huu-Tap Van, Thi Minh Phuong Nguyen: writing – review & editing.

Conflicts of interest

The authors have not disclosed any competing interests.

Data availability

The data associated with this study have not been deposited in a publicly available repository. Data will be made available on request.

Acknowledgements

This research is funded by the Ministry of Education and Training (MOET), Vietnam under grant number B2025-TNA-08.

References

1 M. Mezzelani, S. Gorbi and F. Regoli, *Mar. Environ. Res.*, 2018, **140**, 41–60.
2 M. Shen, Y. Hu, K. Zhao, C. Li, B. Liu, M. Li, C. Lyu, L. Sun and S. Zhong, *Toxics*, 2023, **11**, e966.
3 Y. Liu, R. Guo, J. Li, Y. Cheng, C. Wang, W. Wang and H. Zheng, *Separations*, 2025, **12**, e15.
4 B. M. Al-howri, S. Ismail and M. Khajavian, *Environ. Monit. Assess.*, 2025, **197**, e1095.
5 B. Xu, H. Zhu, Y. Dai, H. Zhang, Z. Qian, M. Pu, F. Tadayuki, W. Qiu, R. Sun, M. Zhao and X. Zheng, *Environ. Res.*, 2026, **294**, e123830.
6 Y. Liu, M. Xu, L. Feng, L. Zhao, S. He and L. Wei, *Water Res.*, 2026, **288**, e124733.
7 V. Rilstone, Y. Filion and P. Champagne, *Environ. Syst. Res.*, 2025, **14**, e7.
8 T. Manasfi, in *Analysis and Formation of Disinfection Byproducts in Drinking Water*, ed. J.-L. Boudenne, Elsevier, 2021, vol. 92, pp. 85–116.
9 M. Mahmoodi and E. Pishbin, *Environ. Sci. Pollut. Res.*, 2025, **32**, 3531–3570.
10 F. Sarra and M. Bali, *Euro-Mediterr. J. Environ. Integr.*, 2025, **11**, e13.
11 T. Macsek, P. Krzeminski, M. Umar, T. Halešová, D. Tomešová, M. Novotný and P. Hlavínek, *J. Hazard. Mater.*, 2025, **489**, e137703.
12 J. Liu, X. Yuan, H. Dong and C. Sans, *J. Environ. Manage.*, 2025, **383**, e125493.
13 E. Issaka, J. Baffoe and M. Adams, *Sustainable Chem. Environ.*, 2024, **8**, e100185.
14 L. Li, H. Dong, H. Li, L. Sun, F. Pan and X. Yuan, *Sep. Purif. Technol.*, 2023, **324**, e124590.
15 J. Serafin, R. Bujaldón, J. Sreńscek-Nazzal, A. Kałamaga, E. Gomez, X. Vendrell and A. Serra, *Chem. Eng. J.*, 2025, **524**, e169005.
16 C. Gong, X. Lv, S. Liu, X. Chen, R. Weerasooriya and Z. Ding, *J. Ind. Eng. Chem.*, 2025, **141**, 340–350.
17 M. Zhan, M. Xu, W. Lin, H. He and C. He, *Nanomaterials*, 2025, **15**, e507.
18 H. Wang, Z. Xu and X. Yang, *Carbon*, 2025, **233**, e119831.
19 S. Garg, in *Nanocomposites for Sustainable Wastewater Treatment*, ed. S. Roy, S. Garg and C. W. Lai, Springer Nature Singapore, Singapore, 2025, pp. 25–44.
20 M. Tanemura, S. Sharma, W. M. Lin, T. Akiyama, M. Z. M. Yusop and Y. Yang, in *Woodhead Publishing Series in Electronic and Optical Materials*, ed. P. Chakraborty and D. Mohanta, Woodhead Publishing, 2026, vol. 2, pp. 1–24.
21 Z. Cheng, Q. Meng, X. Jiang, S. Gun and L.-S. Fan, *Discover Energy*, 2025, **5**, e20.
22 N. Li, J. Xu, W. Gao, S. Wan, X. Xu, B. Yan, J. Wang and G. Chen, *Chem. Eng. J.*, 2026, **528**, e172413.
23 X. Chen, G. Lu, H. Zhang and J. Wan, *Sci. Rep.*, 2026, **16**, e4776.
24 H. Sun, G. Xu, W. Lian, G. Kastiukas, J. Zhang, X. Zhang, W. Liu, F. Xing and J. Ren, *Chem. Phys. Lett.*, 2022, **786**, e139206.
25 R. T. Schossler, S. Ojo, Z. Jiang, J. Hu and X. Yu, *Sci. Rep.*, 2024, **14**, 1–15.
26 Z. Song, M. Wang, Z. Wang, Y. Wang, R. Li, Y. Zhang, C. Liu, L. Ye, B. Xu and F. Qi, *Environ. Sci. Technol.*, 2019, **53**, 5337–5348.
27 Y. Cheng, J. Kang, P. Yan, J. Shen, Z. Chen, X. Zhu, Q. Tan, L. Shen, S. Wang and S. Wang, *Appl. Catal., B*, 2024, **341**, e123325.
28 G. Ponnusamy, H. Farzaneh, Y. Tong, J. Lawler, Z. Liu and J. Saththasivam, *Sci. Rep.*, 2021, **11**, e6342.
29 Q. Wang, Y. Ji, J. Hu, H. Ye, Y. Liu, Y. Wang, C. Chen and Z. Li, *Front. Environ. Sci.*, 2022, **10**, 1–11.
30 W. Wu, L. Bai, Y. Song, Y. Su, K. Jiang, H. Sun, G. Zhen, Y. Shen, Q. Yuan and Z. Sun, *ACS Appl. Mater. Interfaces*, 2021, **13**, 52706–52716.
31 L. Sánchez, B. E. Huayta, P. G. Ramos and J. Rodríguez, *J. Phys.: Conf. Ser.*, 2022, **2172**, e12013.
32 J. Martini, C. A. Orge, J. L. Faria, M. F. R. Pereira and O. S. G. P. Soares, *Appl. Sci.*, 2019, **9**, e2652.

33 Y. He, M. Chen, J. Wang, G. Zhao, S. Han, X. Yang, Y. Chen, C. Wang and J. Wang, *J. Chem. Educ.*, 2023, **100**, 3556–3563.
34 J. Rivera-Utrilla, M. V. López-Ramón, M. Sánchez-Polo, M. A. Álvarez and I. Velo-Gala, *Catalysts*, 2020, **10**, e1485.
35 P. Chakartnarodom, N. Kongkajun and W. Prakaypan, *Key Eng. Mater.*, 2017, **751**, 195–201.
36 P. Basnet, D. Samanta, T. Inakhunbi Chanu, J. Mukherjee and S. Chatterjee, *SN Appl. Sci.*, 2019, **1**, e633.
37 P. A. Luque, A. Lopez-Peraza, O. J. Nava-Olivas, G. A. Parra, Y. Báez-López, V. M. Orozco-Carmona, H. E. Garrafa-Gálvez and M. J. Chinchillas-Chinchillas, *Materials*, 2021, **14**, e7537.
38 F. Atikah, B. Yuliarto and R. V. Manurung, *J. Phys.: Conf. Ser.*, 2024, **2705**, e12009.
39 M. E. Naghani, M. Neghabi, M. Zadsar and H. A. Ahangar, *Sci. Rep.*, 2023, **13**, e1496.
40 S. H. EL-Moslamy, A. H. Rezk, M. Elkady and H. Shokry, *Arabian J. Sci. Eng.*, 2024, **49**, 9067–9088.
41 N. Hao, P. Cao, Q. Shi, C. Song, Y. Lv and T. Peng, *Nanomaterials*, 2025, **15**, e383.
42 T. N. Reddy, J. Manna and R. K. Rana, *ACS Appl. Mater. Interfaces*, 2015, **7**, 19684–19690.
43 G. Shukla, M. Rani and U. Shanker, in *Graphene–Metal Oxide Composites: Synthesis, Properties, and Applications*, ed. S. Moharana, S. K. Satpathy, T. A. Nguyen and T. Maharana, Royal Society of Chemistry, 2025, pp. 1–30.
44 S. P. Onkani, P. N. Diagboya, S. O. Akpotu and F. M. Mtunzi, *Ind. Eng. Chem. Res.*, 2025, **64**, 11815–11825.
45 D. Yang, F. Meng, Z. Zhang and X. Liu, *ACS Omega*, 2023, **8**, 21823–21829.
46 X. Tao, Y. Cui and Z. Liu, *Water*, 2024, **16**, e1274.
47 A. Yulikasari, E. Nurhayati, F. X. F. Cornelio and D. Susanti, *Sustinere: J. Environ. Sustainability*, 2023, **7**, 39–47.
48 V. H. Hoang, T. H. H. Chu, T. D. Nguyen, N. T. H. Vien, T. H. Nguyen, T. C. Luu, H. T. Van, H. Nguyen, D. T. Duong and V. H. L. Nguyen, *Korean J. Chem. Eng.*, 2024, **41**, 1415–1425.
49 K. P. V. Lekshmi, S. Yesodharan and E. P. Yesodharan, *Eur. Chem. Bull.*, 2017, **6**, e177.
50 S. Ghosh and B. B. Saha, *J. Compos. Sci.*, 2023, **7**, e207.
51 T. G. Gindose, G. Gebreslassie, T. D. Hailegebreal, T. G. Ashebr, F. M. Mtunzi, T. B. Atisme and E. A. Zereffa, *RSC Adv.*, 2024, **14**, 38459–38469.
52 X. Wang, F. Yuan, D. Xue, J. Liu, J. Wei, Y. Wang, J. Wang, Q. Qu and Q. Zhang, *Chemnanomat*, 2022, **8**, e202200243.
53 M. Jiang, M. Shi, J. Li, J. Liu, L. Zhang, J. Qin, Y. Jiu, B. Tang and D. Xu, *Microelectron. Int.*, 2022, **39**, 166–174.
54 S. A. David and C. Vedhi, *ECS Trans.*, 2022, **107**, 2003–2021.
55 S. Shao, T. Cheng, Y. Cheng and B. Chen, *RSC Adv.*, 2024, **14**, 30990–31002.
56 M. M. A. daiem, J. Rivera-Utrilla, R. Ocampo-Pérez, J. D. Méndez-Díaz and M. Sánchez-Polo, *J. Environ. Manage.*, 2012, **109**, 164–178.
57 M. Li, L. Fu, L. Deng, Y. Hu, Y. Yuan and C. Wu, *Environ. Sci. Ecotechnol.*, 2023, **15**, e100244.
58 D. Zuo, Y. Yin, L. Jiang, Z. Xia, C. Tan, J. Li, J. Zuo and Y. Wang, *Coatings*, 2024, **14**, e192.
59 R. O. Z. Brohi, M. Y. Khuhawar, R. B. Mahar, M. Ibrahim, A. Ali and M. F. Lanjwani, *J. Chem. Technol. Biotechnol.*, 2022, **97**, 3406–3418.
60 I. Mukherjee, V. Cilamkoti and R. K. Dutta, *ACS Appl. Nano Mater.*, 2021, **4**, 7686–7697.
61 S. Nekouei, F. Nekouei and H. Kargarzadeh, *Appl. Organomet. Chem.*, 2017, **32**, e4198.
62 B. Shili, O. Khaldi, C. Mendes-Felipe, M. Rosales, D. C. Alves, P. M. Martins, R. Ben Younès and S. Lanceros-Méndez, *Nanomaterials*, 2025, **15**, e1307.
63 M. Wang, G. Zhang, S. Dong, N. Li, Q. Xu, H. Li, J. Lu and D. Chen, *Adv. Funct. Mater.*, 2024, **34**, e2406516.
64 E. Dhanaraman, A. Verma, P. Chen, N. Chen, Y. Siddiqui and Y. Fu, *Sol. RRL*, 2024, **8**, e2300981.
65 C. M. Morrison, S. Hogard, R. Pearce, A. Mohan, A. N. Pisarenko, E. Dickenson, U. von Gunten and E. C. Wert, *Environ. Sci. Technol.*, 2023, **57**, 18393–18409.
66 L. Luo, Z. Sun, Y. Chen, H. Zhang, Y. Sun, D. Lu and J. Ma, *RSC Adv.*, 2023, **13**, 1906–1913.
67 B. D. Boruah and A. Misra, *ACS Energy Lett.*, 2017, **2**, 1720–1728.